

Low-Altitude UAV Tracking via Sensing-Assisted Predictive Beamforming

Yifan Jiang, Qingqing Wu, Hongxun Hui, Wen Chen, and Derrick Wing Kwan Ng

Abstract—Sensing-assisted predictive beamforming, as one of the enabling technologies for emerging integrated sensing and communication (ISAC) paradigm, shows significant promise for enhancing various future unmanned aerial vehicle (UAV) applications. However, current works on sensing-assisted predictive beamforming predominately emphasized on spectral efficiency enhancement, while the impact of such beamforming techniques on the communication reliability was largely unexplored and challenging to characterize. To fill this research gap and tackle this issue, this paper investigates outage capacity maximization for UAV tracking under the sensing-assisted predictive beamforming scheme. Specifically, a cellular-connected UAV tracking scheme is proposed leveraging extended Kalman filtering (EKF), where the predicted UAV trajectory, sensing duration ratio, and target constant received signal-to-noise ratio (SNR) are jointly optimized to maximize the outage capacity at each time slot. To address the implicit nature of the objective function, closed-form approximations of the outage probabilities (OPs) at both prediction and measurement stages of each time slot are proposed based on second-order Taylor expansions, providing an efficient and full characterization of outage capacity. Subsequently, an efficient algorithm is proposed based on a combination of bisection search and successive convex approximation (SCA) to address the non-convex optimization problem with guaranteed convergence. To further reduce computational complexity, a second efficient algorithm is developed based on alternating optimization (AO). Simulation results validate the accuracy of the derived OP approximations, the effectiveness of the proposed algorithms, and the significant outage capacity enhancement over various benchmarks. Furthermore, we show that the optimized predicted UAV trajectory tends to be parallel to the base station’s uniform linear array antennas with a nonzero minimum distance, indicating a trade-off between decreasing path loss and enjoying wide beam coverage for outage capacity maximization.

Index Terms—Integrated sensing and communication (ISAC), unmanned aerial vehicle (UAV), tracking, low-altitude, outage, sensing-assisted predictive beamforming.

I. INTRODUCTION

The production of unmanned aerial vehicles (UAVs), also known as drones, is anticipated to experience sustained rapid growth over the next decade, reaching a global market value of over 70 billion dollars by 2030 [1]. To date, the realizations of numerous emerging applications have been facilitated by

Yifan Jiang is with the State Key Laboratory of Internet of Things for Smart City, University of Macau, Macao 999078, China (email: yc27495@umac.mo) and also with Shanghai Jiao Tong University, Shanghai 200240, China. Qingqing Wu and Wen Chen are with the Department of Electronic Engineering, Shanghai Jiao Tong University, Shanghai 200240, China (e-mail: {qingqingwu@sjtu.edu.cn; wenchen@sjtu.edu.cn}). Hongxun Hui is with the State Key Laboratory of Internet of Things for Smart City and Department of Electrical and Computer Engineering, University of Macau, Macao, 999078 China (email: hongxunhui@um.edu.mo). Derrick Wing Kwan Ng is with the School of Electrical Engineering and Telecommunications, University of New South Wales, Sydney, NSW 2052, Australia (e-mail: w.k.ng@unsw.edu.au).

UAVs’ superior mobility and flexible maneuverability, including logistics, remote sensing, environmental detection, industrial monitoring, border surveillance, and emergency communication [2]. Moreover, the emerging low-altitude economy (LAE) has attracted significant worldwide attention with the aim of achieving unprecedently efficient utilization of vertical space below an altitude of 1000 meters for both existing and future applications, such as precise agriculture and air taxis [3]–[5]. However, it can be envisioned that signal interference and network congestion will intensify considerably due to the explosive increase in UAV equipment. Under these challenging circumstances, it is crucial to guarantee the communication and tracking performance of UAV users and targets, since these metrics serve the foundations for the aforementioned applications. In addition, despite the independent progress made in UAV communication and tracking, such as short packet communication and global navigation satellite system [2], incompatibility among standalone systems designed for different functions causes inefficient use of hardware and spectrum resources, which degrades overall system performance.

In recent years, integrated sensing and communication (ISAC) has been proposed and widely investigated as an enabling technology for the upcoming sixth-generation (6G) network [6]–[8]. By effectively utilizing the inherent reciprocity between sensing and communication, ISAC is expected to offer more precise and reliable wireless coverage for UAVs, thereby mitigating signal interference among multiple UAVs and enabling a greater number of UAVs to simultaneously access the network. Meanwhile, hardware and spectrum resources can be efficiently integrated, significantly reducing system overhead and improving overall spectral efficiency. In addition, benefitting from the widely deployed terrestrial wireless network infrastructure, a large number of base stations (BSs) and distributed antennas can effectively serve as communication or sensing nodes, enabling considerable signal enhancement and seamless UAV coverage. Therefore, ISAC technologies present a vital solution to address the aforementioned issues, while simultaneously providing high-quality communication and tracking services for UAVs.

Among various existing signal processing and architecture designs for ISAC, sensing-assisted predictive beamforming is appealing due to its effectiveness in enhancing both target tracking accuracy and communication links for users concurrently [9]–[11]. Specifically, sensing-assisted predictive beamforming refers to the design of beamforming vectors based on both predicted and measured user information, typically user directions or positions. Indeed, the prediction of user directions or positions can be completed prior to the measurement

from received echo signals. As such, the overhead associated with channel estimation or beam tracking, such as pilots, as well as the latency in acquiring user information can be considerably reduced. Additionally, predicted and measured user information can be jointly utilized to improve sensing accuracy compared to conventional schemes that exploit only the measurement results from the perspective of Bayesian filtering [11]. As a result, significant system performance enhancement can be achieved by sensing-assisted predictive beamforming across various ISAC-enabled applications in vehicular [10]–[20] and UAV [21]–[23] networks.

Existing studies on sensing-assisted predictive beamforming for communication performance enhancement mainly focused on the spectral efficiency improvement [10], [12]–[18], [22], [23]. For instance, a predictive beamforming framework leveraging extended Kalman filtering (EKF) was proposed for beam tracking for vehicular communications, achieving a promising achievable rate enhancement over conventional feedback-based communication schemes [10]. In [12]–[18], predictive beamforming-based approaches were proposed to improve the achievable sum-rate of multiple vehicles in vehicular networks. Moreover, sensing-assisted predictive beamforming designs were proposed to track eavesdroppers in secure communication scenarios, thereby enhancing the secrecy rates of legitimate users [22], [23]. However, spectral efficiency is insufficient for characterizing the performance in reliable communication scenarios with severe channel fading and stringent reliability requirements [24]–[26]. Instead, some other fundamental communication performance metrics, such as beam misalignment probability, outage probability (OP), and outage capacity, are more appropriate for characterizing the communication reliability. Relatively few investigations examined improvements in beam misalignment probability brought by sensing-assisted predictive beamforming [11], [19], [20]. Specifically, the impact of beamwidth on the beam misalignment probability was studied in [11] for predictive beamforming-enabled vehicle tracking. Furthermore, dynamic beamwidth designs for vehicle tracking were proposed to guarantee the tracking accuracy [19] or to maximize the beam misalignment probability-weighted achievable rate [20]. Nevertheless, beam misalignment probability only partially characterizes the received signal strength reliability, while OP and outage capacity fully characterize the reliability of link capacity and remain largely uncharacterized under sensing-assisted predictive beamforming frameworks. Without proper characterization, the roles of prediction and measurement in sensing-assisted predictive beamforming on communication reliability cannot be sufficiently understood. In addition, such characterization is challenging due to the intractable channel fading probability distribution.

Moreover, unlike vehicles and standalone UAVs whose trajectories cannot be participated in the overall system designs, the trajectories of cellular-connected UAVs can be designed and jointly optimized with other system resources for maximizing the overall system performance [2], [27], [28]. Particularly, for predictive beamforming-enabled cellular-connected UAV tracking, the UAV trajectory can only be partially designed due to the inherently random environmental

variations and control errors in practice [2], [28], [29]. In this condition, the cellular-connected UAV trajectory/movement can significantly affect the tracking and communication performance, since the Cramér-Rao bounds (CRBs) for UAV position/movement estimation are highly dependent on the spatial relationship between the UAV and the BS [7], [30], [31]. Consequently, the BS/cellular-connected UAV trajectory optimization for maximizing the overall system reliability-aware communication performance, e.g., outage capacity, under the sensing-assisted predictive beamforming framework remains an open and crucial issue to be addressed.

Motivated by the aforementioned issues, we investigate the outage capacity characterization and maximization via UAV trajectory optimization in this paper. Specifically, a cellular-connected UAV is served and also concurrently tracked via EKF by a monostatic ISAC BS. Through remote control from the BS, the predicted UAV trajectory can be proactively controlled, although it is interfered by control noise modeled as a Gaussian random process. Within each short time slot, the UAV motion state is assumed to be deterministic yet unknown in advance. Meanwhile, the communication performance directly depends on a sensing duration ratio between the prediction and measurement durations at each time slot under the sensing-assisted predictive beamforming scheme. As a result, the system communication reliability at each time slot can be evaluated by OPs and outage capacities at the prediction and measurement stages, respectively. The main contributions of this paper are summarized as follows:

- A joint UAV tracking and outage capacity maximization scheme is proposed for reliable communication, where an optimization problem for outage capacity maximization is formulated and addressed at each time slot to optimize the predicted UAV trajectory, sensing duration ratio, and target constant received signal-to-noise ratios (SNRs), subject to constraints on UAV velocity and a maximum tolerable OP.
- To address the implicit and non-convex objective function and constraints in the formulated problem, closed-form approximations of OPs for both the prediction and measurement stage are proposed based on second-order Taylor expansions, enabling the full characterization of outage capacity and a more tractable optimization problem formulation. To the best of our knowledge, this paper represents the first effort to characterize the outage capacity under the sensing-assisted predictive beamforming scheme in ISAC systems.
- An efficient algorithm is proposed to handle the formulated optimization problem with guaranteed convergence, in which the formulated problem is decomposed into two feasibility problems addressed by the bisection search and SCA, respectively. Moreover, the updating rules between the two feasibility problems are heuristically designed based on the proved monotonicity of approximated OPs with respect to (w.r.t.) the target constant received SNRs. To further reduce computational complexity and avoid unnecessary trials involving infeasible solutions, a second efficient algorithm is proposed capitalizing alternating

optimization (AO), which maximizes the outage capacity within a few iterations.

- Simulation results validate the effectiveness of our proposed OP approximations, algorithms, and outage capacity maximization scheme. In addition, in the prediction mean square error (MSE)-dominant case, our proposed joint UAV tracking and outage capacity maximization scheme achieves a significant outage capacity improvement compared to benchmarks. Moreover, our results reveal that the optimized predicted UAV trajectory ends up with being parallel to the BS uniform linear array (ULA) antennas with a nonzero minimum distance, which also demonstrates a trade-off between reducing path loss and enlarging beam coverage area to maximize the outage capacity.

Notation: $\mathbf{0}_m$ and $\mathbf{1}_m$ denote a $m \times 1$ column vector with all elements equal to 0 and 1, respectively. \mathbb{R} denotes the set of real numbers. $\mathcal{O}(\cdot)$ represents the big-O notation for computational complexity. $\mathbb{E}_x[\cdot]$ is statistical expectation w.r.t. the distribution of x . $\mathcal{N}(\mathbf{x}, \mathbf{Q})$ denotes a real-valued Gaussian distribution with a mean vector \mathbf{x} and covariance matrix \mathbf{Q} and \sim means “distributed as”. \prec is the element-wise component inequality. \arctan denotes the arctangent function. \otimes is the Kronecker product. $\text{diag}(b_1, \dots, b_L)$ denotes a diagonal matrix with b_1, \dots, b_L being its diagonal elements. For an arbitrary matrix \mathbf{A} , \mathbf{A}^T , \mathbf{A}^{-1} , $\det(\mathbf{A})$, and $[\mathbf{A}]_{ij}$ denote its transpose, inverse, determinant, and (i, j) -th element, respectively. For a real-valued continuous function $f(\mathbf{x}; y, z)$, $\nabla_{\mathbf{x}} f(\mathbf{x}; y, z)$ represents the gradient of $f(\mathbf{x}; y, z)$ w.r.t. the vector \mathbf{x} given the values of y and z . $\frac{dy}{dx}$ and $\frac{\partial y}{\partial x}$ denote the derivative and the partial derivative of the variable y w.r.t. the variable x , respectively.

II. SYSTEM MODEL

We consider a terrestrial BS that employs ISAC signals to simultaneously track and communicate with a single-antenna cellular-connected UAV.¹ As an initial study, it is assumed that the UAV flies at a fixed altitude of H m, and the BS is equipped with ULAs comprising N_t transmit antennas and N_r receive antennas.² Furthermore, the uncertainty of the UAV motion state (i.e., the UAV position and velocity) is considered owing to practical issues such as control errors [28]. Moreover, with a sufficiently short time interval ΔT s, the UAV motion state can be assumed to be invariant [32]. Therefore, without loss of generality, a three-dimensional (3D) Cartesian coordinate system is considered, where the BS is located at the origin and the UAV motion state vector at the n -th time slot can be denoted by $\mathbf{x}_n = [x_n, v_n^x, y_n, v_n^y]^T$

¹The considered scenario can be readily extended to multi-UAV scenarios, where the BS serves multiple UAVs with time-division or frequency-division multiple access schemes. The extension to cases with spatial-division multiple access is non-trivial due to the inter-beam interference and thus worthwhile future works.

²This model can be readily extended to the case with 3D trajectory optimization by incorporating the altitude into the state vector. The extensions to cases with other types of antenna arrays are challenging due to complicated beam patterns, requiring dedicated future works. To avoid deviation from the emphasis of outage capacity characterization and maximization, this paper studies the case with the mentioned system configurations.

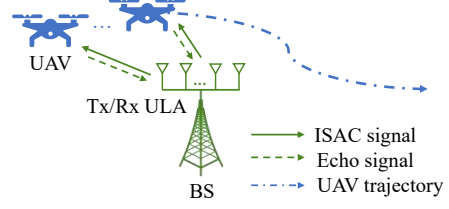


Fig. 1. System model illustration.

with x_n , v_n^x , y_n , and v_n^y denoting the x -axis coordinate, the velocity along x -axis, the y -axis coordinate, and the velocity along y -axis, respectively. Despite the inherent uncertainty in UAV motion state, it is still possible to partially plan the UAV trajectory by designing the predicted state vector at the $(n+1)$ -th time slot, which can be realized by remote control from the BS [27], [28]. The UAV mobility model and other parts of our considered system are specified in the following subsections.

A. UAV Mobility Model

The entire UAV flight dynamic can be described exploiting a discrete-time state evolution model expressed as [30], [33], [34]

$$\mathbf{x}_n = \mathbf{G}\mathbf{x}_{n-1} + \mathbf{u}_n + \mathbf{z}_{p,n}, \forall n \in \{1, 2, \dots, N\}, \quad (1)$$

where $\mathbf{G} \in \mathbb{R}^{4 \times 4}$ denotes the transition matrix, $\mathbf{u}_n \in \mathbb{R}^{4 \times 1}$ denotes the motion control input from the BS, N denotes the total number of time slots, and $\mathbf{z}_{p,n} \sim \mathcal{N}(\mathbf{0}, \mathbf{Q}_p)$ denotes the process noise owing to control errors [33], respectively. The expressions of \mathbf{G} and $\mathbf{Q}_p \in \mathbb{R}^{4 \times 4}$ can be given by

$$\mathbf{G} = \mathbf{I}_2 \otimes \begin{bmatrix} 1 & \Delta T \\ 0 & 1 \end{bmatrix}, \mathbf{Q}_p = \mathbf{I}_2 \otimes \begin{bmatrix} \frac{1}{3} \Delta T^3 & \frac{1}{2} \Delta T^2 \\ \frac{1}{2} \Delta T^2 & \Delta T \end{bmatrix} \tilde{q}, \quad (2)$$

, respectively, where \tilde{q} denotes the process noise intensity.³

Note that $\{\mathbf{x}_n\}, \forall n$, is indeed a random process and cannot be directly acquired by either the UAV or the BS. Fortunately, \mathbf{x}_n can be predicted at the $(n-1)$ -th time slot and subsequently estimated at the n -th time slot, which are denoted by $\check{\mathbf{x}}_n = [\check{x}_n, \check{v}_n^x, \check{y}_n, \check{v}_n^y]^T$ and $\hat{\mathbf{x}}_n = [\hat{x}_n, \hat{v}_n^x, \hat{y}_n, \hat{v}_n^y]^T$, respectively. More specifically, by designing the motion control input as $\mathbf{u}_n = \check{\mathbf{x}}_n - \mathbf{G}\hat{\mathbf{x}}_{n-1}$, the relationship between \mathbf{x}_n and $\check{\mathbf{x}}_n$ can be compactly expressed as

$$\mathbf{x}_n = \check{\mathbf{x}}_n + \mathbf{G}(\mathbf{x}_{n-1} - \hat{\mathbf{x}}_{n-1}) + \mathbf{z}_{p,n}. \quad (3)$$

Therefore, the UAV trajectory optimization can be performed by appropriately optimizing $\check{\mathbf{x}}_n$. The detailed procedures for obtaining $\hat{\mathbf{x}}_n$ are dependent on $\check{\mathbf{x}}_n$ and are specified in the following subsection. Furthermore, a crucial assumption about the prediction and estimation errors is specified as follows:

Assumption 1 (Small prediction/estimation error): In this paper, we assume that the prediction and estimation errors, although inherently exist and follow different probability distributions, are sufficiently small. Thus, the ground-truth value of the state vector can be approximated by the predicted and estimated values, i.e., $\mathbf{x}_n \approx \check{\mathbf{x}}_n \approx \hat{\mathbf{x}}_n$ [10], [31], [35].

Remark 1: Although assumption 1 may appear idealistic, small prediction and estimation errors are practically

³ \mathbf{G} and \mathbf{Q}_p can be derived by sampling a continuous-time random process modelling the UAV movement as in [30], [33], [34].

achievable in scenarios such as millimeter-wave ISAC systems. Specifically, highly accurate localization/tracking can be achieved thanks to favorable channel conditions and large antenna array gain [11]–[13], [20]. Moreover, this study primarily focuses on characterizing the impact of UAV trajectories on communication reliability under the sensing-assisted predictive beamforming scheme. Therefore, assumption 1 is well-justified and does not diminish the necessity and value of the proposed investigation.

B. Sensing-Assisted Beamforming

In our considered ISAC system, a two-stage predictive beamforming scheme is implemented by the BS to achieve real-time UAV tracking and communication [10]–[13], [20], [22]. At each stage, the BS adaptively designs its beamforming vector according to the predicted or estimated UAV motion state, which is detailed as follows:

1) *Prediction Stage*: At the beginning w_n ratio of the n th time slot, the BS generates the predicted state vector $\check{\mathbf{x}}_n$ and the beamforming vector $\hat{\mathbf{f}}_n = \mathbf{a}(\hat{\theta}_n) = \mathbf{a}(\arctan(\check{y}_n/\check{x}_n))$, where w_n and $\hat{\theta}_n$ denote the sensing duration ratio and the predicted azimuth angle, respectively. Based on assumption 1, predictive beamforming can achieve sufficient accuracy such that the UAV is reliably illuminated by the main lobe of the beam, enabling the BS to successfully receive echo signals from the UAV. Meanwhile, the BS measures the azimuth angle θ_n and distance d_n of the UAV. The measurement model is explicitly given by

$$\mathbf{w}_n = \mathbf{h}(\mathbf{x}_n) + \mathbf{z}_{m,n} \quad (4)$$

$$= \begin{bmatrix} \arctan(y_n/x_n) \\ \sqrt{x_n^2 + y_n^2 + H^2} \end{bmatrix} + \begin{bmatrix} z_{1,n} \\ z_{2,n} \end{bmatrix}, \quad (5)$$

where $\mathbf{w}_n = [\hat{\theta}_n, \hat{d}_n]^T$ represents the measured results, $\hat{\theta}_n$ denotes the measured azimuth angle, \hat{d}_n denotes the measured distance, $\mathbf{z}_{m,n}$ represents the measurement noise vector with $z_{i,n} \sim \mathcal{N}(0, \sigma_{i,n}^2)$, $i = 1, 2$, and $\sigma_{i,n}^2, i = 1, 2$ denote the corresponding measurement noise variance, respectively. Given the sparse blockages and scatterings in the vertical dimension, the communication channel between the BS and UAV can be assumed to be line-of-sight (LoS)-dominant with free-space path loss [27], [32], [36]. Consequently, the expressions of $\sigma_{i,n}^2, i = 1, 2$ are given by

$$\sigma_{1,n}^2 = \frac{a_1^2(x_n^2 + y_n^2 + H^2)^2(x_n^2 + y_n^2)}{\rho_r w_n y_n^2}, \quad (6)$$

$$\sigma_{2,n}^2 = \frac{a_2^2(x_n^2 + y_n^2 + H^2)^2}{\rho_r w_n}, \quad (7)$$

and the measurement noise covariance matrix for $\mathbf{z}_{m,n}$ can be derived as $\mathbf{Q}_{m,n} = \text{diag}(\sigma_{1,n}^2, \sigma_{2,n}^2)$. In (6) and (7), $a_i, i = 1, 2$ represent the corresponding measurement capability coefficients calculated according to the system configurations and signal processing designs [10], [31], [35], [37], and $\rho_r \in \mathbb{R}$ denotes the sensing power gain coefficient given by [38]

$$\rho_r = \frac{P_A N_{\text{sym}} N_t N_r}{\sigma^2} \left(\frac{\sigma_{\text{RCS}} \lambda^2}{(4\pi)^3} \right), \quad (8)$$

where P_A denotes the BS transmit power, N_{sym} is matched-filtering gain accumulated during the whole time slot, σ^2 de-

notes the additive white Gaussian noise power at the receiver, σ_{RCS} signifies the target radar cross-section, and λ denotes the carrier wavelength [30].

2) *Estimation Stage*: During the remaining duration of the n th time slot, the BS completes its measurement and obtains the estimated state vector denoted by $\hat{\mathbf{x}}_n$ following the standard EKF procedures [34], given by the following steps.

a) Obtaining the predicted state vector $\check{\mathbf{x}}_n$.

b) Linearization: $\mathbf{H}_n = \frac{\partial \mathbf{h}}{\partial \mathbf{x}_n}|_{\mathbf{x}_n=\check{\mathbf{x}}_n}, \forall n$.

c) Calculating the prediction MSE matrix:

$$\mathbf{M}_{p,n} = \mathbf{G} \mathbf{M}_{n-1} \mathbf{G}^H + \mathbf{Q}_p. \quad (9)$$

d) Calculating the Kalman gain matrix:

$$\mathbf{K}_n = \mathbf{M}_{p,n} \mathbf{H}_n^H (\mathbf{Q}_{m,n} + \mathbf{H}_n \mathbf{M}_{p,n} \mathbf{H}_n^H)^{-1}. \quad (10)$$

e) Obtaining the estimated state vector:

$$\hat{\mathbf{x}}_n = \check{\mathbf{x}}_n + \mathbf{K}_n (\mathbf{w}_n - \mathbf{h}(\check{\mathbf{x}}_n)). \quad (11)$$

f) Calculating the estimation MSE matrix:

$$\mathbf{M}_n = (\mathbf{I} - \mathbf{K}_n \mathbf{H}_n) \mathbf{M}_{p,n} = (\mathbf{H}_n^H \mathbf{Q}_{m,n}^{-1} \mathbf{H}_n + \mathbf{M}_{p,n}^{-1})^{-1}. \quad (12)$$

The detailed derivation of (12) can be referred to [10]. In (10) and (12), the expression of \mathbf{H}_n is given by

$$\mathbf{H}_n = \begin{bmatrix} -\frac{\check{y}_n}{\check{x}_n^2 + \check{y}_n^2} & 0 & \frac{\check{x}_n}{\check{x}_n^2 + \check{y}_n^2} & 0 \\ \frac{\check{x}_n}{\sqrt{\check{x}_n^2 + \check{y}_n^2 + H^2}} & 0 & \frac{\check{y}_n}{\sqrt{\check{x}_n^2 + \check{y}_n^2 + H^2}} & 0 \end{bmatrix}. \quad (13)$$

Finally, the BS designs its transmit beamforming vector as $\hat{\mathbf{f}}_n = \mathbf{a}(\hat{\theta}_n) = \mathbf{a}(\arctan(\hat{y}_n/\hat{x}_n))$.

C. Outage Capacity Characterization

Given the considered predictive beamforming scheme and channel model, the instantaneous achievable rate at the prediction and estimation stages of the n th time slot can be represented by

$$R_{p,n} = \log_2 (1 + \gamma_{p,n}) = \log_2 \left(1 + \frac{\tilde{P} |\mathbf{a}(\theta_n)^H \mathbf{a}(\check{\theta}_n)|}{x_n^2 + y_n^2 + H^2} \right), \quad (14)$$

$$R_{e,n} = \log_2 (1 + \gamma_{e,n}) = \log_2 \left(1 + \frac{\tilde{P} |\mathbf{a}(\theta_n)^H \mathbf{a}(\hat{\theta}_n)|}{x_n^2 + y_n^2 + H^2} \right), \quad (15)$$

respectively, where the coefficient \tilde{P} is defined as $\tilde{P} \triangleq P_A \beta_0 / \sigma^2$ and $\beta_0 = (\lambda/4\pi)^2$ represents the channel power gain at the reference distance of 1 m. Additionally, $\gamma_{p,n}$ and $\gamma_{e,n}$ denotes the SNR at the corresponding stage, respectively. Then, because of the assumed invariant actual UAV motion state within ΔT s and the dominated LoS path, the random factors in $R_{p,n}$ and $R_{e,n}$, i.e., $\frac{|\mathbf{a}(\theta_n)^H \mathbf{a}(\check{\theta}_n)|}{x_n^2 + y_n^2 + H^2}$ and $\frac{|\mathbf{a}(\theta_n)^H \mathbf{a}(\hat{\theta}_n)|}{x_n^2 + y_n^2 + H^2}$, respectively, can be modeled as slow flat fading with a coherence time of ΔT s [25]. Therefore, the OPs at the prediction and estimation stage of the n th time slot are expressed as

$$\zeta_{p,n} = \mathbb{P}(\xi_{p,n} < 0), \quad \zeta_{e,n} = \mathbb{P}(\xi_{e,n} < 0), \quad (16)$$

where $\xi_{p,n}$ and $\xi_{e,n}$ are defined as $\xi_{p,n} \triangleq \gamma_{p,n} - \check{\gamma}_n$ and $\xi_{e,n} \triangleq \gamma_{e,n} - \hat{\gamma}_n$, respectively. Here, $\check{\gamma}_n$ and $\hat{\gamma}_n$ are the target constant received SNRs at the prediction and estimation stages of the n th time slot, satisfying $\zeta_{p,n} = \varepsilon_{\text{out}}$ and $\zeta_{e,n} = \varepsilon_{\text{out}}$ ⁴

⁴It is intractable to obtain closed-form expressions of $\zeta_{p,n}$ and $\zeta_{e,n}$. To address this issue, the values of $\zeta_{p,n}$ and $\zeta_{e,n}$ satisfying $\zeta_{p,n} = \varepsilon_{\text{out}}$ and $\zeta_{e,n} = \varepsilon_{\text{out}}$ can be searched based on our proposed approximations and algorithms in Section III and IV, respectively.

respectively, where ε_{out} denotes the maximum tolerable OP [24]. Furthermore, the outage capacities normalized by the bandwidth at the prediction and estimation stage are given by

$$C_{\text{p},n} = \log_2 (1 + \check{\gamma}_n), \quad C_{\text{e},n} = \log_2 (1 + \hat{\gamma}_n), \quad (17)$$

respectively. As such, the overall outage capacity at the n th time slot can be represented by $C_n = w_n C_{\text{p},n} + (1 - w_n) C_{\text{e},n}$.

D. Problem Formulation

In this paper, we propose a joint UAV tracking and outage capacity maximization scheme. To be specific, the predicted UAV trajectory $\check{\mathbf{q}}_n = [\check{x}_n, \check{y}_n]^T$, sensing duration ratio w_n and target constant received SNR vector $\gamma_n = [\check{\gamma}_n, \hat{\gamma}_n]^T$ are jointly optimized to maximize the overall outage capacity at each time slot. The corresponding optimization problem is formulated as

$$(\text{P1}) : \max_{\{\check{\mathbf{q}}_n, w_n, \gamma_n\}} C_n \quad (18)$$

$$\text{s.t. } \|\check{\mathbf{q}}_n - \hat{\mathbf{q}}_{n-1}\| \leq v_{\text{A,max}} \Delta T, \quad (18a)$$

$$\check{y}_n \geq y_{\min}, \quad (18b)$$

$$w_{\min} \leq w_n \leq w_{\max}, \quad (18c)$$

$$\kappa(\check{\mathbf{q}}_n, w_n, \gamma_n) \leq 0, \quad (18d)$$

$$\mathbf{0} \prec \gamma_n \prec \gamma_{\max} \mathbf{1}_2, \quad (18e)$$

where $\hat{\mathbf{q}}_{n-1} = [\hat{x}_{n-1}, \hat{y}_{n-1}]^T$ denotes the estimated UAV trajectory at the $(n-1)$ -th time slot, $v_{\text{A,max}}$ denotes the UAV maximum velocity, $\kappa(\check{\mathbf{q}}_n, w_n, \gamma_n) = \max(\zeta_{\text{p},n}, \zeta_{\text{e},n}) - \varepsilon_{\text{out}}$ represents the maximum OP at the n th time slot and $\gamma_{\max} = \tilde{P}N_{\text{t}}/(y_{\min}^2 + H^2)$ denotes the maximum target constant received SNR due to the maximum beamforming gain and the minimum path loss, respectively. In (P1), (18a) represents the maximum UAV velocity constraint, while (18b) represents a minimum y -axis coordinate constraint of a flyable zone.⁵ (18c), (18d) and (18e) denote the sensing duration ratio range, maximum tolerable OP, and SNR range constraints, respectively. (P1) is challenging to be optimally solved since the objective function is non-convex and constraint (18d) is generally implicit.

III. PROPOSED OP APPROXIMATIONS

To address the implicit and challenging constraint (18d) in (P1), approximations of OP at both the prediction and estimation stages are proposed. These approximations not only make solving (P1) tractable but also provide analytical expressions characterizing the outage performance of the considered sensing-assisted beamforming scheme.

A. Prediction Stage

Let us denote the ground-truth UAV trajectory by $\mathbf{q}_n = [x_n, y_n]^T$. Then, based on assumption 1, it can be reasonably inferred that the UAV is consistently illuminated by the main lobe of the downlink transmitted beam thanks to the small

⁵In practice, the UAV position with $\check{y}_n = 0$ leads to the infinite azimuth angle measurement noise variance. Thus, we consider a case where the UAV trajectory is constrained in an area with a nonzero minimum y -axis coordinate denoted by $y_{\min} > 0$.

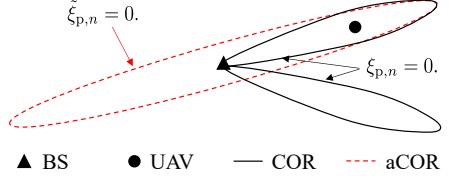


Fig. 2. A geometric illustration of COR and aCOR.

prediction/estimation error. As a result, the beamforming gain from the BS can be expressed as

$$|\mathbf{a}(\theta_n)^H \mathbf{a}(\check{\theta}_n)| = \frac{\sin\left(\frac{N_{\text{t}}\pi}{2}\kappa(\mathbf{q}_n; \check{\mathbf{q}}_n)\right)}{\sin\left(\frac{\pi}{2}\kappa(\mathbf{q}_n; \check{\mathbf{q}}_n)\right)}, \quad (19)$$

where the expression of $\kappa(\mathbf{q}_n; \check{\mathbf{q}}_n)$ is given by

$$\begin{aligned} \kappa(\mathbf{q}_n; \check{\mathbf{q}}_n) &\triangleq \cos(\check{\theta}_n) - \cos(\theta_n) \\ &= \frac{\check{x}_n}{\sqrt{\check{x}_n^2 + \check{y}_n^2}} - \frac{x_n}{\sqrt{x_n^2 + y_n^2}}. \end{aligned} \quad (20)$$

As such, at the prediction stage, the complementary outage event, i.e., the event that the UAV does not experience signal outage, can be formulated as

$$\frac{\sin\left(\frac{N_{\text{t}}\pi}{2}\kappa(\mathbf{q}_n; \check{\mathbf{q}}_n)\right)}{\sin\left(\frac{\pi}{2}\kappa(\mathbf{q}_n; \check{\mathbf{q}}_n)\right)} \geq \frac{\check{\gamma}_n(x_n^2 + y_n^2 + H^2)}{\tilde{P}}. \quad (21)$$

From the geometric perspective, condition (21) defines a region on the (x_n, y_n) -plane given the fixed altitude H , namely the complementary outage region (COR) as shown in Fig. 2. Correspondingly, the complementary OP can be calculated by integrating the probability density function (PDF) of \mathbf{q}_n over COR. However, the left-hand side (LHS) of (21) is intractable for the integral and overly complicated for the Taylor expansion w.r.t. $\check{\mathbf{q}}_n$. To tackle this issue, we propose a two-step approximation with procedures detailed as follows.

In the first step, the LHS of (21) is approximated by its second-order Taylor expansion w.r.t. the function $\kappa(\cdot)$ at the point $\check{\kappa}_n = 0$, yielding:

$$\frac{\sin\left(\frac{N_{\text{t}}\pi}{2}\kappa(\mathbf{q}_n; \check{\mathbf{q}}_n)\right)}{\sin\left(\frac{\pi}{2}\kappa(\mathbf{q}_n; \check{\mathbf{q}}_n)\right)} \approx N_{\text{t}} - M\kappa(\mathbf{q}_n; \check{\mathbf{q}}_n)^2, \quad (22)$$

with $M = \frac{N_{\text{t}}\pi^2(N_{\text{t}}^2 - 1)}{24}$. Then, the outage event (21) can be approximated by

$$\kappa(\mathbf{q}_n; \check{\mathbf{q}}_n)^2 + \frac{\check{\gamma}_n(x_n^2 + y_n^2 + H^2)}{\tilde{P}M} - \frac{N_{\text{t}}}{M} \geq 0. \quad (23)$$

In (23), the function $\kappa(\mathbf{q}_n; \check{\mathbf{q}}_n)$ remains challenging to handle due to its fractional structure. Thus, the second step is to approximate the LHS of (23) by the second-order Taylor expansion w.r.t. the ground-truth UAV trajectory \mathbf{q}_n at the point $\mathbf{q}_n = \check{\mathbf{q}}_n$ and reformulate (23) as

$$\tilde{\xi}_{\text{p},n} = \frac{1}{2}\dot{\mathbf{q}}_n^T \tilde{\xi}_{\text{p},n}^{(2)} \dot{\mathbf{q}}_n + (\tilde{\xi}_{\text{p},n}^{(1)})^T \dot{\mathbf{q}}_n + \tilde{\xi}_{\text{p},n}^{(0)} \geq 0, \quad (24)$$

where $\dot{\mathbf{q}}_n$ is defined by $\dot{\mathbf{q}}_n \triangleq \mathbf{q}_n - \check{\mathbf{q}}_n = [\dot{x}_n, \dot{y}_n]^T$ representing the deviation of predicted UAV trajectory from the ground-truth UAV trajectory, $\tilde{\xi}_{\text{p},n}^{(2)}$ and $\tilde{\xi}_{\text{p},n}^{(1)}$ denote the Hessian matrix and gradient of the LHS of (23) w.r.t. the ground-truth UAV trajectory \mathbf{q}_n , respectively. The specific expressions of

$$\check{\chi}_{\text{U}}(\dot{x}_n) = \frac{\check{\Lambda}_{\text{x},n}^2 \dot{y}_{\text{U}}(\dot{x}_n) - \check{\Lambda}_{\text{xy},n}^2 \dot{x}_n}{\sqrt{2|\det(\check{\Lambda}_n)|\check{\Lambda}_{\text{x},n}}}, \check{\chi}_{\text{L}}(\dot{x}_n) = \frac{\check{\Lambda}_{\text{x},n}^2 \dot{y}_{\text{L}}(\dot{x}_n) - \check{\Lambda}_{\text{xy},n}^2 \dot{x}_n}{\sqrt{2|\det(\check{\Lambda}_n)|\check{\Lambda}_{\text{x},n}}}, \dot{x}_{\text{U}} = -\dot{x}_n + \sqrt{-\frac{Y_1}{Y_2}}, \dot{x}_{\text{L}} = -\dot{x}_n - \sqrt{-\frac{Y_1}{Y_2}}, \quad (31)$$

$$\dot{y}_{\text{U}}(\dot{x}_n) = -\dot{y}_n + Y_0(\dot{x}_n + \dot{x}_n) + \sqrt{Y_1 + Y_2(\dot{x}_n + \dot{x}_n)^2}, \dot{y}_{\text{L}}(\dot{x}_n) = -\dot{y}_n + Y_0(\dot{x}_n + \dot{x}_n) - \sqrt{Y_1 + Y_2(\dot{x}_n + \dot{x}_n)^2}, \quad (32)$$

$$Y_0 = \frac{\dot{x}_n \dot{y}_n^3 \tilde{P} M}{(\dot{x}_n^2 + \dot{y}_n^2)^3 \gamma + \dot{x}_n^2 \dot{y}_n^2 \tilde{P} M}, Y_1 = \frac{(\tilde{P} N_{\text{t}} - H^2 \gamma)(\dot{x}_n^2 + \dot{y}_n^2)^3}{(\dot{x}_n^2 + \dot{y}_n^2)^3 \gamma + \dot{x}_n^2 \dot{y}_n^2 \tilde{P} M}, Y_2 = -\frac{(\dot{x}_n^2 + \dot{y}_n^2)^4 ((\dot{x}_n^2 + \dot{y}_n^2)^2 \gamma^2 + \tilde{P} M \dot{y}_n^2 \gamma)}{((\dot{x}_n^2 + \dot{y}_n^2)^3 \gamma + \dot{x}_n^2 \dot{y}_n^2 \tilde{P} M)^2}, \quad (33)$$

$\tilde{\xi}_{\text{p},n}^{(2)}$, $\tilde{\xi}_{\text{p},n}^{(1)}$ and $\tilde{\xi}_{\text{p},n}^{(0)}$ are given by

$$\tilde{\xi}_{\text{p},n}^{(2)} = \begin{bmatrix} 2\xi_n^{(20)} & \xi_n^{(11)} \\ \xi_n^{(11)} & 2\xi_n^{(02)} \end{bmatrix}, \quad \tilde{\xi}_{\text{p},n}^{(1)} = \begin{bmatrix} \xi_n^{(10)} \\ \xi_n^{(01)} \end{bmatrix}, \quad (25)$$

with

$$\tilde{\xi}_n^{(20)} = \frac{\dot{y}_n^4}{(\dot{x}_n^2 + \dot{y}_n^2)^3} + \frac{\dot{\gamma}_n}{M \tilde{P}}, \quad \tilde{\xi}_n^{(11)} = \frac{-2\dot{x}_n \dot{y}_n^3}{(\dot{x}_n^2 + \dot{y}_n^2)^3}, \quad (26)$$

$$\tilde{\xi}_n^{(02)} = \frac{\dot{x}_n^2 \dot{y}_n^2}{(\dot{x}_n^2 + \dot{y}_n^2)^3} + \frac{\dot{\gamma}_n}{M \tilde{P}}, \quad \tilde{\xi}_n^{(10)} = \frac{2\dot{\gamma}_n \dot{x}_n}{M \tilde{P}}, \quad (27)$$

$$\tilde{\xi}_n^{(01)} = \frac{2\dot{\gamma}_n \dot{y}_n}{M \tilde{P}}, \quad \tilde{\xi}_{\text{p},n}^{(0)} = \frac{(\dot{x}_n^2 + \dot{y}_n^2 + H^2)\dot{\gamma}_n}{\tilde{P} M} - \frac{N_{\text{t}}}{M}. \quad (28)$$

Since it can be easily obtained that $\tilde{\xi}_n^{(20)} \tilde{\xi}_n^{(02)} - (\tilde{\xi}_n^{(11)}/2)^2 > 0$ holds if $\dot{\gamma}_n > 0$ is satisfied, the approximated COR (aCOR) boundary, denoted by $\tilde{\xi}_{\text{p},n} = 0$, represents an ellipse on the (\dot{x}_n, \dot{y}_n) plane, and thus is tractable for integral calculation, as illustrated in Fig. 2. Besides, (26)-(28) show that the aCOR boundary largely depends on the predicted UAV trajectory $\dot{\mathbf{q}}_n$, indicating that the outage capacity can be maximized by optimizing the predicted UAV trajectory. Consequently, our proposed approximated OP at the prediction stage of the n th time slot is provided in the following proposition.

Proposition 1: Given assumption 1, the OP at the prediction stage of the n th time slot can be approximated by

$$\zeta_{\text{p},n} \approx \tilde{\zeta}_{\text{p},n} = 1 - \mathbb{E}_{\dot{x}_n} [\tilde{\chi}(\dot{x}_n)], \quad (29)$$

with

$$\tilde{\chi}(\dot{x}_n) \triangleq \begin{cases} \frac{\operatorname{erf}(\tilde{\chi}_{\text{U}}(\dot{x}_n)) - \operatorname{erf}(\tilde{\chi}_{\text{L}}(\dot{x}_n))}{2}, & \dot{x}_n \in [\dot{x}_{\text{L}}, \dot{x}_{\text{U}}], \\ 0, & \text{Otherwise,} \end{cases} \quad (30)$$

where \dot{x}_n follows a zero mean Gaussian distribution with a variance of $\check{\Lambda}_{\text{x},n}^2 = [\mathbf{M}_{\text{p},n}]_{11}$. The specific expressions of $\tilde{\chi}_{\text{U}}(\cdot)$, $\tilde{\chi}_{\text{L}}(\cdot)$, \dot{x}_{U} , and \dot{x}_{L} are given by (31)-(33), respectively.

Proof: Please refer to Appendix A. \blacksquare

B. Estimation Stage

Let us denote the estimated UAV trajectory at the n th time slot by $\hat{\mathbf{q}}_n = [\hat{x}_n, \hat{y}_n]^T$ and define $\dot{\mathbf{q}}_n$ as $\dot{\mathbf{q}}_n \triangleq \mathbf{q}_n - \hat{\mathbf{q}}_n = [\dot{x}_n, \dot{y}_n]^T$. Then, similar as the derivation process from (19) to (24), the COR at the estimation stage of the n th time slot can be approximated by

$$\tilde{\xi}_{\text{e},n} = \frac{1}{2} \dot{\mathbf{q}}_n^T \tilde{\xi}_{\text{e},n}^{(2)} \dot{\mathbf{q}}_n + (\tilde{\xi}_{\text{e},n}^{(1)})^T \dot{\mathbf{q}}_n + \xi_{\text{e},n}^{(0)}, \quad (34)$$

where $\xi_{\text{e},n}^{(0)}$ is given by $\xi_{\text{e},n}^{(0)} = \frac{(\dot{x}_n^2 + \dot{y}_n^2 + H^2)\dot{\gamma}_n}{\tilde{P} M} - \frac{N_{\text{t}}}{M}$, $\tilde{\xi}_{\text{e},n}^{(2)}$ and $\tilde{\xi}_{\text{e},n}^{(1)}$ are given by $\tilde{\xi}_{\text{e},n}^{(2)} = \tilde{\xi}_{\text{p},n}^{(2)}|_{\dot{\mathbf{q}}_n = \hat{\mathbf{q}}_n, \dot{\gamma}_n = \dot{\gamma}_n}$ and $\tilde{\xi}_{\text{e},n}^{(1)} = \tilde{\xi}_{\text{p},n}^{(1)}|_{\dot{\mathbf{q}}_n = \hat{\mathbf{q}}_n, \dot{\gamma}_n = \dot{\gamma}_n}$, respectively. However, it is generally intractable to directly calculate $\tilde{\xi}_{\text{e},n}$ at the $(n-1)$ th time slot,

since calculating $\xi_{\text{e},n}^{(0)}$, $\tilde{\xi}_{\text{e},n}^{(1)}$, and $\tilde{\xi}_{\text{e},n}^{(2)}$ requires the knowledge of \hat{x}_n and \hat{y}_n , which become available only after receiving the echo signals at the n th time slot. To address this issue, the approximation $\dot{\mathbf{q}}_n \approx \check{\mathbf{q}}_n$ is reasonably applied given assumption 1. Thus, $\tilde{\xi}_{\text{e},n}$ can be further approximated by

$$\tilde{\xi}_{\text{e},n} \approx \tilde{\xi}_{\text{ea},n} = \frac{1}{2} \dot{\mathbf{q}}_n^T \tilde{\xi}_{\text{ea},n}^{(2)} \dot{\mathbf{q}}_n + (\tilde{\xi}_{\text{ea},n}^{(1)})^T \dot{\mathbf{q}}_n + \xi_{\text{ea},n}^{(0)}, \quad (35)$$

with $\tilde{\xi}_{\text{ea},n}^{(2)} = \tilde{\xi}_{\text{p},n}^{(2)}|_{\dot{\gamma}_n = \dot{\gamma}_n}$, $\tilde{\xi}_{\text{ea},n}^{(1)} = \tilde{\xi}_{\text{p},n}^{(1)}|_{\dot{\gamma}_n = \dot{\gamma}_n}$ and $\tilde{\xi}_{\text{ea},n}^{(0)} = \tilde{\xi}_{\text{p},n}^{(0)}|_{\dot{\gamma}_n = \dot{\gamma}_n}$, which can be calculated at the $(n-1)$ th time slot. Meanwhile, similar as the derivation process in the proof of Proposition 1, $\dot{\mathbf{q}}_n \sim \mathcal{N}(\mathbf{0}, \hat{\Lambda}_n)$ approximately holds with

$$\hat{\Lambda}_n = \begin{bmatrix} \hat{\Lambda}_{\text{x},n}^2 & \hat{\Lambda}_{\text{xy},n}^2 \\ \hat{\Lambda}_{\text{xy},n}^2 & \hat{\Lambda}_{\text{y},n}^2 \end{bmatrix} \approx \begin{bmatrix} [\mathbf{M}_n]_{11} & [\mathbf{M}_n]_{13} \\ [\mathbf{M}_n]_{31} & [\mathbf{M}_n]_{33} \end{bmatrix}, \quad (36)$$

and the OP at the estimation stage of the n th time slot can be approximated by

$$\zeta_{\text{e},n} \approx \tilde{\zeta}_{\text{e},n} = 1 - \mathbb{E}_{\dot{x}_n} [\tilde{\chi}(\dot{x}_n)], \quad (37)$$

with

$$\tilde{\chi}(\dot{x}_n) \triangleq \begin{cases} \frac{\operatorname{erf}(\tilde{\chi}_{\text{U}}(\dot{x}_n)) - \operatorname{erf}(\tilde{\chi}_{\text{L}}(\dot{x}_n))}{2}, & \dot{x}_n \in [\dot{x}_{\text{L}}, \dot{x}_{\text{U}}], \\ 0, & \dot{x}_n \in (-\infty, \dot{x}_{\text{L}}) \cup (\dot{x}_{\text{U}}, \infty). \end{cases} \quad (38)$$

The expressions of functions $\tilde{\chi}_{\text{U}}(\dot{x}_n)$ and $\tilde{\chi}_{\text{L}}(\dot{x}_n)$ are given by

$$\tilde{\chi}_{\text{U}}(\dot{x}_n) = \frac{\hat{\Lambda}_{\text{x},n}^2 \dot{y}_{\text{U}}(\dot{x}_n) - \hat{\Lambda}_{\text{xy},n}^2 \dot{x}_n}{\sqrt{2|\det(\hat{\Lambda}_n)|\hat{\Lambda}_{\text{x},n}}}, \quad (39)$$

$$\tilde{\chi}_{\text{L}}(\dot{x}_n) = \frac{\hat{\Lambda}_{\text{x},n}^2 \dot{y}_{\text{L}}(\dot{x}_n) - \hat{\Lambda}_{\text{xy},n}^2 \dot{x}_n}{\sqrt{2|\det(\hat{\Lambda}_n)|\hat{\Lambda}_{\text{x},n}}}, \quad (40)$$

with $\dot{x}_{\text{L}} = \dot{x}_{\text{L}}|_{\dot{\gamma}_n = \dot{\gamma}_n}$, $\dot{x}_{\text{U}} = \dot{x}_{\text{U}}|_{\dot{\gamma}_n = \dot{\gamma}_n}$, $\dot{y}_{\text{L}} = \dot{y}_{\text{L}}|_{\dot{\gamma}_n = \dot{\gamma}_n}$ and $\dot{y}_{\text{U}} = \dot{y}_{\text{U}}|_{\dot{\gamma}_n = \dot{\gamma}_n}$, respectively.⁶

IV. PROPOSED ALGORITHMS

Given the approximated OPs presented in (29) and (37), (P1) can be reformulated into an approximated optimization problem as:

$$(P2) : \max_{\{\dot{\mathbf{q}}_n, w_n, \gamma_n\}} C_n \quad (41)$$

$$\text{s.t. (18a)-(18c), (18e),} \quad (41a)$$

$$\tilde{\varkappa}(\dot{\mathbf{q}}_n, w_n, \gamma_n) \leq 0, \quad (41a)$$

with $\tilde{\varkappa}(\dot{\mathbf{q}}_n, w_n, \gamma_n) = \max(\tilde{\zeta}_{\text{p},n}, \tilde{\zeta}_{\text{e},n}) - \varepsilon_{\text{out}}$. Compared with (P1), the original implicit constraint (18d) in (P1) has been replaced by the approximated outage constraint (41a). However, (P2) remains challenging to be optimally solved

⁶Although the COR seems to be quite different from the aCOR in Fig. 2, the approximations still achieve satisfactory accuracies thanks to assumption 1, which will be further verified in Section V.

due to non-convex constraint (41a) and the coupling among the optimization variables. To address this issue, an algorithm based on bisection search is proposed to obtain an efficient solution to (P2) with guaranteed convergence. To further reduce computational complexity, a second efficient algorithm is proposed based on AO.

A. Search-Based Algorithm

To decouple $\check{\mathbf{q}}_n$ from w_n and γ_n , our proposed search-based algorithm solves (P2) by iteratively solving two subproblems formulated as

$$(P2.1) : \text{Find } w_n, \gamma_n \quad (42)$$

$$\text{s.t. (18c), (18e),}$$

$$C_n = C_i, \quad (42a)$$

and

$$(P2.2) : \min_{\check{\mathbf{q}}_n} \tilde{\chi}(\check{\mathbf{q}}_n, w_i, \gamma_i) \quad \text{s.t. (18a), (18b),}$$

respectively, where C_i denotes a given objective value in the i -th iteration, and (w_i, γ_i) denotes the solution to (P2.1). To be specific, our proposed search-based algorithm solves (P2.1) to generate a candidate solution (w_i, γ_i) and subsequently evaluate its feasibility to (P2) by solving (P2.2) in the i -th iteration. If $\tilde{\chi}(\check{\mathbf{q}}_i, w_i, \gamma_i) < 0$ holds with $\check{\mathbf{q}}_i$ denoting the solution to (P2.2), $(\check{\mathbf{q}}_i, w_i, \gamma_i)$ constitutes a feasible solution to (P2), and a larger objective value can be given in the $(i+1)$ -th iteration to maximize the outage capacity. However, it is intractable to exhaustively check the feasibility of all solutions to (P2.1). Moreover, it is challenging to design the updating rule of the given objective value in the $(i+1)$ -th iteration without loss of optimality to (P2) since the function $\tilde{\chi}(\check{\mathbf{q}}_n, w_n, \gamma_n)$ is complicated and non-convex. To tackle this issue, our proposed search-based algorithm heuristically designs the subalgorithm for (P2.1) and the updating rule of the given objective value based on the monotonicity of $\tilde{\chi}(\check{\mathbf{q}}_n, w_n, \gamma_n)$ w.r.t. γ_n given in the following proposition.

Proposition 2: Given any feasible $\check{\mathbf{q}}_i$ and w_i to (P2), the function $\tilde{\chi}(\check{\mathbf{q}}_i, w_i, \gamma_n)$ is a monotonically nondecreasing function of γ_n . ■

Proof: Please refer to Appendix B. ■

Proposition 2 indicates that it is easier to identify feasible solutions to (P2) with smaller target constant received SNRs. Let $\mathcal{S}_i = \{(w_n, \check{\mathbf{q}}_n) | \tilde{\chi}(\check{\mathbf{q}}_n, w_n, \gamma_i) < 0\}$ and $\mathcal{S}'_i = \{(w_n, \check{\mathbf{q}}_n) | \tilde{\chi}(\check{\mathbf{q}}_n, w_n, \gamma'_i) < 0\}$ denote the feasible set for (P2) given γ_i and γ'_i , respectively. Then, if $\gamma_i \succeq \gamma'_i$ is satisfied, $\mathcal{S}_i \subseteq \mathcal{S}'_i$ holds because all the elements in \mathcal{S}_i satisfy $\tilde{\chi}(\check{\mathbf{q}}_n, w_n, \gamma'_i) < \tilde{\chi}(\check{\mathbf{q}}_n, w_n, \gamma_i) < 0$. Thanks to the continuity of $\tilde{\chi}(\check{\mathbf{q}}_n, w_n, \gamma_n)$ w.r.t $\check{\mathbf{q}}_n$ in most parts of COR, the feasible set \mathcal{S}'_i probably contains elements not belonging to \mathcal{S}_i , which further indicates a higher chance of finding a feasible solution to (P2) in \mathcal{S}'_i than in \mathcal{S}_i .

Inspired by this observation, the subalgorithm for (P2.1) is designed as a two-layer bisection search. Note that the feasible set for (P2.1) can be expressed as a set of line segments rotating around the point (C_i, C_i) , which can be divided into two convex sets by considering the cases with $C_{p,n} \geq C_{e,n}$ and $C_{p,n} < C_{e,n}$, respectively. In each case, C_n increases with

γ_n and either increases or decreases with w_n monotonically. Consequently, the bisection search can be applied to obtain a converged solution to (P2.1). To be specific, in each case, $C_{p,n}$ and w_n are searched in the inner and outer layer, respectively, as follows:

1) *Inner layer:* The searched value of $C_{p,n}$ in the k -th iteration, denoted by $C_{p,k}$, is selected from an interval $[C_{p,k}^L, C_{p,k}^U]$, where $C_{p,k}^L$ and $C_{p,k}^U$ denote the lower and upper bounds of $C_{p,k}$, respectively, [39]. Accordingly, the searched value of $C_{e,n}$ in the k -th iteration can be obtained from (42a) and denoted by $C_{e,k}$. Then, the corresponding target constant received SNR vector $\gamma_k = [\check{\gamma}_k, \hat{\gamma}_k]^T$ is obtained by $\check{\gamma}_k = 2^{C_{p,k}} - 1$ and $\hat{\gamma}_k = 2^{C_{e,k}} - 1$. Next, the feasibility of (w_j, γ_k) is checked by substituting $w_i = w_j$ and $\gamma_i = \gamma_k$ into (P2.2), where w_j denotes the searched value of w_n in the j -th iteration of the outer layer. If a predicted UAV trajectory $\check{\mathbf{q}}_k$ satisfying $\tilde{\chi}(\check{\mathbf{q}}_k, w_j, \gamma_k) < 0$ can be obtained, then the solution to (P2.1) is obtained as $(\check{\mathbf{q}}_i, w_i, \gamma_i) = (\check{\mathbf{q}}_k, w_j, \gamma_k)$. Otherwise, if $\tilde{\chi}_{p,n}(\check{\mathbf{q}}_k, w_j, \check{\gamma}_k) \geq 0$ holds, $C_{p,k+1} \in [C_{p,k}^L, C_{p,k}^U]$ is heuristically updated in the $(k+1)$ -th iteration to increase the possibility of finding a predicted UAV trajectory feasible to (P2) based on Proposition 2. If $\tilde{\chi}_{p,n}(\check{\mathbf{q}}_k, w_j, \check{\gamma}_k) \geq 0$ is not satisfied, $\tilde{\chi}_{p,n}(\check{\mathbf{q}}_k, w_j, \hat{\gamma}_k) \geq 0$ must hold and $C_{p,k+1} \in [C_{p,k}^L, C_{p,k}^U]$ is updated in the $(k+1)$ -th iteration so that $C_{e,k+1}$ could be smaller given a fixed C_i . Such updating does not end until a feasible solution to (P2) is found or the search error reaches the tolerance.

2) *Outer layer:* If no feasible solution to (P2) is obtained when the inner-layer search terminates, the searched value of the sensing duration ratio is updated in the outer layer. In the case with $C_{p,n} \geq C_{e,n}$, $w_{j+1} \in [w_j, w_j^U]$ is heuristically updated in the outer layer because a line segment with a larger w_j contains points with smaller $C_{e,n}$ given the same $C_{p,n}$, which possibly facilitates the search for a feasible solution to (P2). Comparatively, $w_{j+1} \in [w_j^L, w_j]$ is updated if the inner-layer search fails to obtain a feasible solution to (P2) in the case with $C_{p,n} < C_{e,n}$.

If the two-layer search still finds no feasible solution to (P2.2), a smaller objective value is given in the $(i+1)$ -th iteration of our proposed algorithm. The search for an appropriate objective value can also be effectively performed via the bisection search.

To address the non-convex objective function in (P2.2), the subalgorithm for (P2.2) applies the SCA technique to efficiently obtain a locally optimal solution [40]. In the m -th iteration, (P2.2) is solved with the objective function replaced by a surrogate function based on the second-order Taylor expansion, given by

$$\begin{aligned} \tilde{\chi}_a(\check{\mathbf{q}}_m; \check{\mathbf{q}}_{m-1}^E, w_j, \gamma_k) &= \tilde{\chi}(\check{\mathbf{q}}_{m-1}^E; w_j, \gamma_k) \\ &+ \nabla \tilde{\chi}(\check{\mathbf{q}}_{m-1}^E; w_j, \gamma_k)^T (\check{\mathbf{q}}_m - \check{\mathbf{q}}_{m-1}^E) \\ &+ Q \|\check{\mathbf{q}}_m - \check{\mathbf{q}}_{m-1}^E\|^2, \end{aligned} \quad (43)$$

where $\check{\mathbf{q}}_{m-1}^E$ denotes the Taylor expansion point in the $(m-1)$ -th iteration and Q is a given positive real number ensuring the convexity of (43). Problem (P2.2) with the objective function replaced by (43) is a convex optimization problem and can be optimally solved by standard numerical convex programming

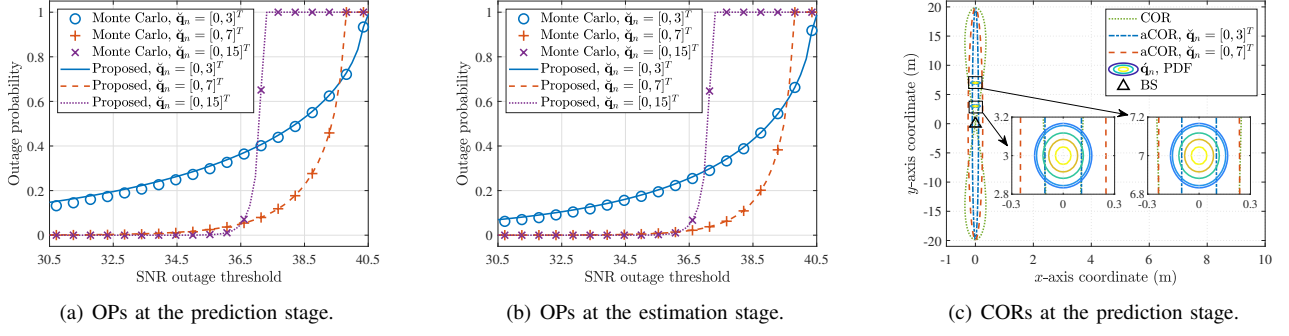


Fig. 3. Accuracies of proposed approximated OPs and CORs under different $\check{\mathbf{q}}_n$.

solvers such as CVX tools [41].

B. AO-Based Algorithm

The computational overhead of our proposed search-based algorithm mainly exists in the subalgorithm solving (P2.2) owing to the complicated objective function. Note that the number of times of solving (P2.2) depends on the inner layer iterations of the two-layer search. However, the searched variables w_j and γ_k may be infeasible to (P2) in each iteration of the inner layer search, leading to an unnecessary trial of solving (P2.2). To significantly reduce these redundant computations, a second algorithm for (P2) is proposed based on the AO method, where the obtained sensing duration ratio and target constant received SNR vector are always feasible to (P2) in each iteration. In this way, the computational complexity of solving (P2) can be reduced.

Given a predicted UAV trajectory $\check{\mathbf{q}}_n = \check{\mathbf{q}}_i$ satisfying (18a) and (18b) in the i -th iteration of our AO-based algorithm, (P2) can be simplified as a subproblem formulated as

$$(P3.1) : \max_{\{w_n, \gamma_n\}} C_n \quad (44)$$

$$\text{s.t. (18c), (18e),}$$

$$\tilde{\gamma}(\check{\mathbf{q}}_i, w_n, \gamma_n) \leq 0. \quad (44a)$$

To handle the non-convex objective function and constraint (44a) in (P3.1), w_n can be heuristically searched by a one-dimensional search, such as the golden section search [42]. As such, the subproblem of (P3.1) given the searched w_n is a convex optimization problem thanks to Proposition 2, and thus can be optimally solved by the bisection search [39]. Then, given the obtained solution to (P3.1) denoted by w_i^* and γ_i^* in the i -th iteration, our proposed algorithm heuristically searches a predicted UAV trajectory $\check{\mathbf{q}}_n$ both feasible to (P2) and possibly resulting in a larger objective value by solving (P2.2) and updates $\check{\mathbf{q}}_{i+1}$ by the obtained solution to (P2.2).

C. Convergence and Computational Complexity Analysis

The computational complexities of our proposed search-based and AO-based algorithm can be analyzed as follows. Specifically, the number of iterations needed for the convergence of the bisection search for w_n and $C_{p,n}$ can be given by $I_w = \log_2(\lfloor (w_{\max} - w_{\min})/\epsilon_w \rfloor)$ and $I_C = \log_2(\lfloor \log_2(1 + \gamma_{\max})/\epsilon_C \rfloor)$, respectively, where ϵ_w and ϵ_C denotes the tolerance of the bisection search for w_n and

$C_{p,n}$, respectively [39]. Thus, the computational complexity of our proposed search-based algorithm can be given by $\mathcal{O}(2I_w I_C^2 J_A)$, where J_A represents the number of iterations needed for the convergence of the SCA to solve (P2.2). In comparison, the computational complexity of our proposed AO-based algorithm can be given by $\mathcal{O}(I'_w I_C + J_A)$, where I'_w denotes the number of iterations needed for the convergence of the one-dimensional search for w_n . Assuming $I_w \approx I'_w$, the computational complexity of our proposed AO-based algorithm is generally lower than that of our search-based algorithm. Nevertheless, the convergence of the search-based algorithm is guaranteed thanks to the guaranteed convergence of the bisection search while the convergence of the AO-based algorithm is not guaranteed owing to the heuristic search for $\check{\mathbf{q}}_n$. To ensure practical applicability, a maximum number of iterations can be predetermined to force the termination of AO-based algorithm.

V. SIMULATION RESULTS

In this section, numerical results are provided to verify the effectiveness of proposed OP approximations and algorithms. Unless specified otherwise, the following system parameters are used: $P_A = 0.1\text{W}$, $\sigma_{\text{RCS}} = 0.2\text{m}^2$, $\lambda = 0.01\text{m}$, $\sigma^2 = -80\text{dBm}$, $H = 50\text{m}$, $\Delta T = 0.02\text{s}$, $v_{A,\max} = 30\text{m/s}$, $N_{\text{sym}} = 10^4$, $N = 10^3$, $w_{\min} = 0.1$, and $w_{\max} = 1$ [31], [43], [44].

A. Proposed OP Approximations

Fig. 3(a) and Fig. 3(b) illustrate the accuracies of our proposed approximated OPs at the prediction and estimation stage, respectively, with three typical predicted UAV positions. Specifically, the Monte Carlo results in Fig. 3(a) and Fig. 3(b) are obtained by simulating the OP results with random noises (including the initial noise, process noise and measurement noise) in one time slot. The number of Monte Carlo simulation runs is set to 10^4 , and other specific system parameters are given by $a_1 = a_2 = 0.1$, $N_t = N_r = 16$, $N = 1$, $w_n = 0.5$ and $M_0 = 10^{-2}\mathbf{I}$ [20], [31], respectively. It can be observed that our proposed OP approximations closely match the Monte Carlo results in the cases with $\check{\mathbf{q}}_n = [0, 7]^T$ and $\check{\mathbf{q}}_n = [0, 15]^T$, thus validating the proposed approximation accuracy and effectiveness.⁷ However, our proposed OP approximations are less accurate in the case with $\check{\mathbf{q}}_n = [0, 3]^T$,

⁷Unless specified otherwise, the OP refers to our proposed approximated OP in following paragraphs for brevity given the verified accuracy.

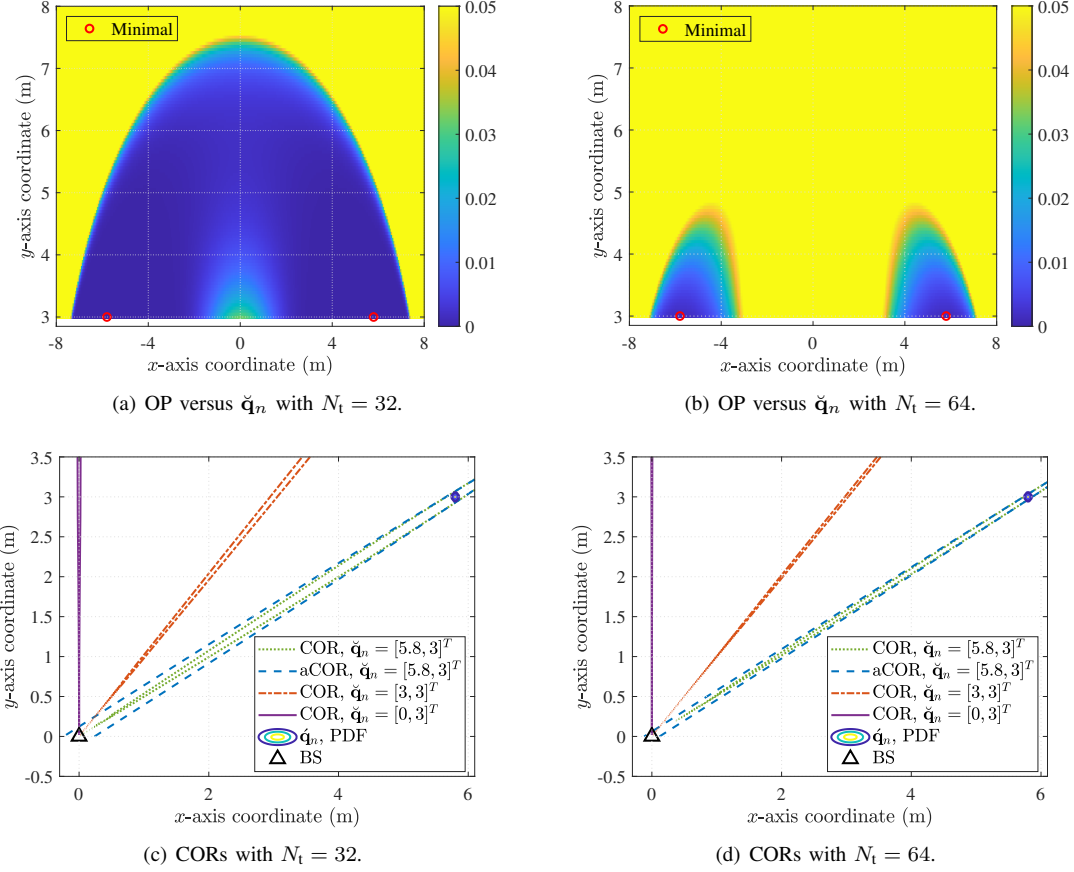


Fig. 4. OPs and CORs with different $\check{\mathbf{q}}_n$ and N_t .

especially at the prediction stage, which indicates that the proposed approximation accuracy is conditional on the UAV position. To explain such property, Fig. 3(c) demonstrates the relationships among the dominant part of $\check{\mathbf{q}}_n$ PDF, COR and aCOR in the cases with $\check{\mathbf{q}}_n = [0, 3]^T$ and $\check{\mathbf{q}}_n = [0, 7]^T$, respectively, given the target constant received SNR $\check{\gamma}_n = 35$. Note that the COR with $\check{\mathbf{q}}_n = [0, 3]^T$ is the same as that with $\check{\mathbf{q}}_n = [0, 7]^T$, since (21) is irrelevant to \check{x}_n and \check{y}_n given $\check{x}_n = 0$. In the scenario with $\check{\mathbf{q}}_n = [0, 7]^T$, despite the seemingly considerable difference between the COR and aCOR, our proposed approximation is still accurate because both the COR and aCOR contain the dominant part of $\check{\mathbf{q}}_n$ PDF, which verifies a condition for our proposed approximation being accurate: *the prediction/estimation error must be sufficiently small such that the difference between COR and aCOR can have negligible impacts on the integral of the highly concentrated $\check{\mathbf{q}}_n$ PDF*. In contrast, in the case with $\check{\mathbf{q}}_n = [0, 3]^T$, both the COR and aCOR intersect with the dominant part of $\check{\mathbf{q}}_n$ PDF, and thereby the difference between the COR and aCOR causes non-negligible approximation accuracy loss. Furthermore, although it is intractable to analytically characterize the relationship between the proposed approximation accuracy and the UAV position, (18b) is considered in this paper as a conservative but efficient constraint on UAV trajectories to avoid the low OP approximation accuracy, such as the case with $\check{\mathbf{q}}_n = [0, 3]^T$.

To obtain important insights into the relationship between the UAV trajectory and OPs, Fig. 4(a) and Fig. 4(b) illustrate the OP at the prediction stage within a given range of $\check{\mathbf{q}}_n$ with

$N_t = 32$ and $N_t = 64$, respectively.⁸ A typically high target constant received SNR is set as $\check{\gamma}_n = 0.975\gamma_{\max}$ for both cases, and other system parameters are specified as: $\mathbf{M}_0 = 10^{-4}\mathbf{I}$, $N = 1$, $y_{\min} = 3$ m and $a_1 = a_2 = 0.1$. As shown in Fig. 4(a) and Fig. 4(b), the optimal predicted UAV trajectories resulting in the minimum OP exist at the line of $\check{y}_n = y_{\min}$, i.e., the minimum distance from the BS, with a certain x -axis coordinate given by ± 5.8 m in both cases. Around the optimal predicted UAV trajectories, there exist certain regions where the OP is relatively low. Compared to the case with $N_t = 32$, the low-OP region with $N_t = 64$ becomes smaller and more concentrated at the optimal predicted UAV trajectories. Also, the positions near the direction $\check{\theta}_n = 0^\circ$ are not contained in the low-OP region with $N_t = 64$. To explain such results, Fig. 4(c) and Fig. 4(d) show the accurate CORs with different predicted UAV trajectories $\check{\mathbf{q}}_n$ corresponding to the cases in Fig. 4(a) and Fig. 4(b), respectively. In both cases, the COR width increases when the predicted UAV trajectory $\check{\mathbf{q}}_n$ varies from the direction $\check{\theta}_n = 90^\circ$ to $\check{\theta}_n = 0^\circ$, which is the main reason why the optimal predicted UAV trajectory $\check{\mathbf{q}}_n^*$ is located at the line of $\check{y}_n = y_{\min}$. However, the UAV should be sufficiently close to the BS due to the potentially severe path loss, and the requirement of letting its dominant part of $\check{\mathbf{q}}_n/\check{\mathbf{q}}_n$ PDF be contained in the COR. Therefore, *the predicted UAV trajectory $\check{\mathbf{q}}_n$ achieves a trade-off between minimizing the path*

⁸The results about the approximated OP at the estimation stage is similar to those at the prediction stage, thus not presented for brevity.

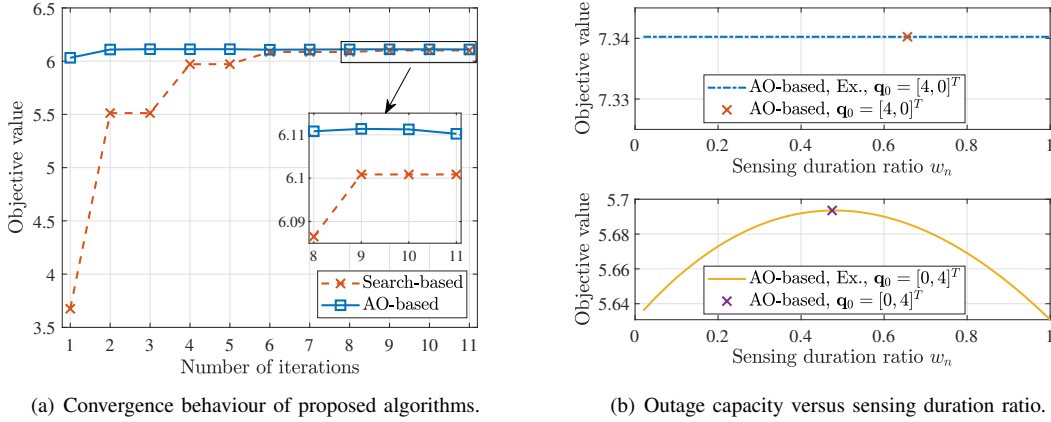


Fig. 5. Performance of proposed algorithms.

loss and being covered by the mainlobe beam for minimizing the OP. Moreover, as illustrated in Fig. 4(a) and Fig. 4(b), the smaller low-OP region with $N_t = 64$ is due to the narrower beam pattern generated by the larger transmit antenna number.

B. Proposed Algorithms

Fig. 5(a) shows the convergence behaviour of our proposed search-based algorithm and AO-based algorithm. The initial state of the UAV is given by $\mathbf{x}_0 = [4, 0, 0, 0]^T$ and the initial estimated state variables are represented by $\hat{\mathbf{x}}_0 = \mathbf{x}_0 + \mathbf{z}_0$ with $\mathbf{z}_0 = [0.083, -0.001, 0.037, 0.042]^T$. The other system parameters are given by: $\varepsilon_{\text{out}} = 10^{-3}$, $a_1 = a_2 = 0.7$, $N_t = N_r = 64$, $N = 1$, and $\mathbf{M}_0 = 10^{-3}\mathbf{I}$. As shown in Fig. 5(a), the convergence of our proposed search-based algorithm is verified and our proposed AO-based algorithm also exhibits satisfactory convergence performance. Although slight fluctuations of the objective values do exist, the objective value obtained by the AO-based algorithm is barely more inaccurate than by the search-based algorithm. This is because the objective value usually varies slightly in the feasible set of (P2), and our proposed AO-based algorithm quickly approaches the near-maximum objective value by solving (P3.1). Therefore, our proposed AO-based algorithm is also effective and has a relatively lower computational complexity than the search-based algorithm.

Fig. 5(b) demonstrates the varying trends of the objective value w.r.t. the sensing duration ratio w_n with different UAV positions. The initial states of the UAV in the two cases are given by $\mathbf{x}_0 = [4, 0, 0, 0]^T$ and $\mathbf{x}_0 = [0, 0, 4, 0]^T$, respectively. The other system parameters are as those in Fig. 5(a) except the OP threshold given by $\varepsilon_{\text{out}} = 10^{-2}$. It can be observed that the impact of w_n on the objective value with $\mathbf{q}_0 = [0, 4]^T$ is much larger than that with $\mathbf{q}_0 = [4, 0]^T$. This is because, when the UAV is at $[0, 4]^T$, the state measurement provides a highly accurate estimation of the UAV trajectory and thus $C_{e,n}$ can be quite larger than $C_{p,n}$. Under such circumstances, the sensing duration ratio w_n achieves a fundamental trade-off between sensing and sensing-assisted communication: when w_n is too small, the matched-filtering gain is insufficient to obtain highly accurate sensing results and thus cannot significantly enhance the communication efficiency or reliability; however, when w_n is exceedingly large, the duration of enjoying the

highly accurate beam alignment from sensing becomes limited, which also leads to sub-optimal communication performance. In contrast to the case with $\mathbf{q}_0 = [0, 4]^T$, the sensing gain is negligible when the UAV is at $[4, 0]^T$ due to the almost infinite measurement noise variance of the azimuth angle, resulting in the minor effect of sensing duration ratio w_n on the objective value. Therefore, when the UAV trajectory is unfavorable to sensing, incorporating the measured results contributes little to the outage capacity enhancement and thus the overhead for real-time state measurement can be saved. Moreover, Fig. 5(b) verifies that a near-optimal solution can be obtained by the subalgorithm for solving (P3.1) of the AO-based algorithm.

C. UAV Trajectories and Communication Performance

In this subsection, the results of our proposed UAV trajectory optimization scheme are compared with those of benchmarks in the prediction MSE-dominant (PMD) and prediction MSE-nondominant (PMnD) case, respectively. In the PMD case, the prediction MSE is so much smaller than the measurement MSE that $\mathbf{K}_n \approx \mathbf{0}$ holds [45], which leads to the estimation MSE dominated by the prediction MSE, i.e., $\mathbf{M}_n \approx \mathbf{M}_{p,n}$, due to (12). Comparatively, the PMnD scenario refers to the case where the prediction MSE is not sufficiently smaller than the measurement MSE to satisfy $\mathbf{K}_n \approx \mathbf{0}$, indicating that the measurement MSE is small and the measured results are useful for decreasing the estimation MSE. In both cases, our proposed UAV trajectory design is compared with the following benchmarks:

- Straight flight and hover (SFH): The UAV directly flies towards a specific position denoted by \mathbf{q}_F with its maximum velocity $v_{A,\max}$ and then hovers at \mathbf{q}_F [46].
- Posterior Cramér-Rao bound (PCRB) minimization (m-PCRB): At each time slot, the UAV trajectory is optimized to minimize the sum of predicted PCRBs for state variables of the next time slot, which can be expressed as [8], [44]

$$\min_{\tilde{\mathbf{q}}_n} \text{Tr}(\mathbf{M}_n |_{\mathbf{x}_n = \tilde{\mathbf{x}}_n}) \quad \text{s.t. (18a).}$$

- $\tilde{\sigma}_{1,n}^2$ minimization (m- $\tilde{\sigma}_{1,n}^2$): At each time slot, the UAV trajectory is optimized to minimize the approximated measurement noise variance for azimuth angle θ_n of the

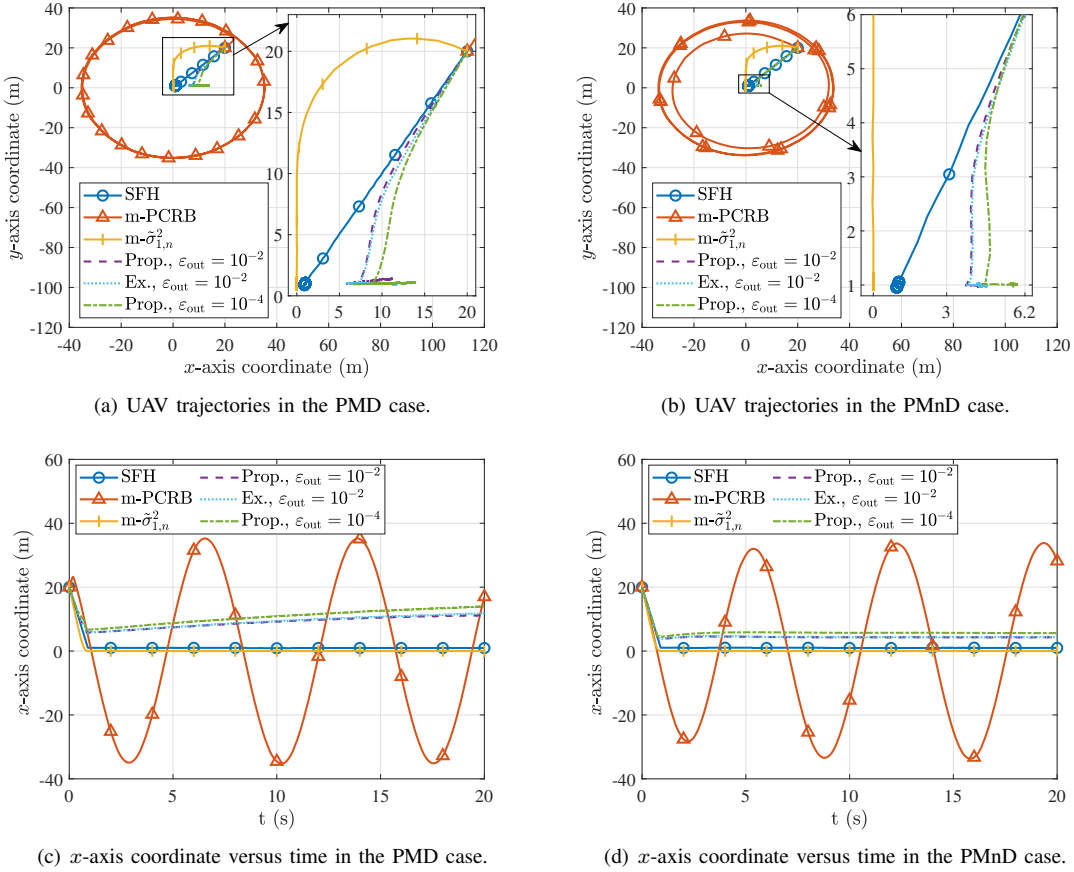


Fig. 6. UAV trajectory comparisons between the PMD and PMnD case.

next time slot denoted by $\tilde{\sigma}_{1,n}^2 = \sigma_{1,n}^2|_{\mathbf{x}_n=\check{\mathbf{x}}_n}$, which can be expressed as

$$\min_{\tilde{\mathbf{q}}_n} \tilde{\sigma}_{1,n}^2 \text{ s.t. (18a), (18b).}$$

The sensing duration ratio w_n is given by $w_{\max} = 1$ to ensure the sensing performance as much as possible for all benchmarks.

1) *UAV trajectories:* Fig. 6(a)-6(d) illustrate the UAV trajectories obtained by the benchmarks and our proposed UAV trajectory optimization scheme in both the PMD and PMnD cases. The measurement capability coefficients are set as $a_1 = a_2 = 1$ and $a_1 = a_2 = 0.1$ for the PMD and PMnD case, respectively. To fairly compare our proposed scheme and benchmarks, the constraint (18b) with $y_{\min} = 1$ is also applied in the m- $\tilde{\sigma}_{1,n}^2$ scheme and the specific position under the SFH scheme is given by $\mathbf{q}_F = [1, 1]^T$. Other system parameters are given by $\tilde{q} = 10^{-5}$ and $\mathbf{x}_0 = [20, 0, 20, 0]^T$. First, it can be observed from both Fig. 6(a) and Fig. 6(b) that the UAV trajectory obtained by our proposed AO-based algorithm (denoted by “Prop.” in Fig. 6(a)-6(d)) well match the results obtained by the exhaustive search (denoted by “Ex.” in Fig. 6(a)-6(d)), which validates the effectiveness of our proposed AO-based algorithm. Second, in both the PMD and PMnD cases, the UAV trajectory under the m-PCRB scheme is approximately circular to maintain an optimal distance minimizing the PCRB, while the UAV under the m- $\tilde{\sigma}_{1,n}^2$ scheme approaches the BS in the direction of $\theta_n = 90^\circ$ and then hovers around

$[0, 1]^T$, which is the optimal position for minimizing $\tilde{\sigma}_{1,n}^2$. Different from the UAV trajectories under benchmarks, the UAV under our proposed scheme tends to approach the BS with a relatively smaller azimuth angle and then stay at the straight line with $\check{y}_n = y_{\min}$ parallel to the BS ULA antennas in both the PMD and PMnD cases. The reason for such trajectory is that being at the line with $\check{y}_n = y_{\min}$ leads to wide COR/beam coverage, which is consistent with our previous observation from Fig. 4(a) and Fig. 4(b) and also demonstrates the importance of beam coverage to signal reception reliability. Consequently, the predicted UAV trajectory parallel to the BS ULA antennas with $\check{y}_n = y_{\min}$ is advantageous for outage capacity maximization. In addition, the UAV trajectory with $\epsilon_{\text{out}} = 10^{-4}$ is generally farther away from the BS than that with $\epsilon_{\text{out}} = 10^{-2}$ in both the PMD and PMnD cases, indicating that a larger UAV-BS distance is more beneficial for enhancing the communication reliability.

2) *Outage capacities:* Fig. 7(a) and Fig. 7(b) compare the outage capacities achieved by the benchmarks and our proposed scheme in both cases. Particularly, the outage capacities of benchmarks are calculated by our proposed algorithm for (P3.1) given their optimized predicted UAV trajectories and the OP threshold $\epsilon_{\text{out}} = 10^{-2}$. As illustrated in Fig. 7(a), the communication performances under the SFH and m- $\tilde{\sigma}_{1,n}^2$ scheme exhibit large random variations similar as fast fadings in the PMD case. The reason is that the UAV is improperly near the BS and can be easily away from the COR/beam coverage due to the position uncertainty. The outage capacity under the m-

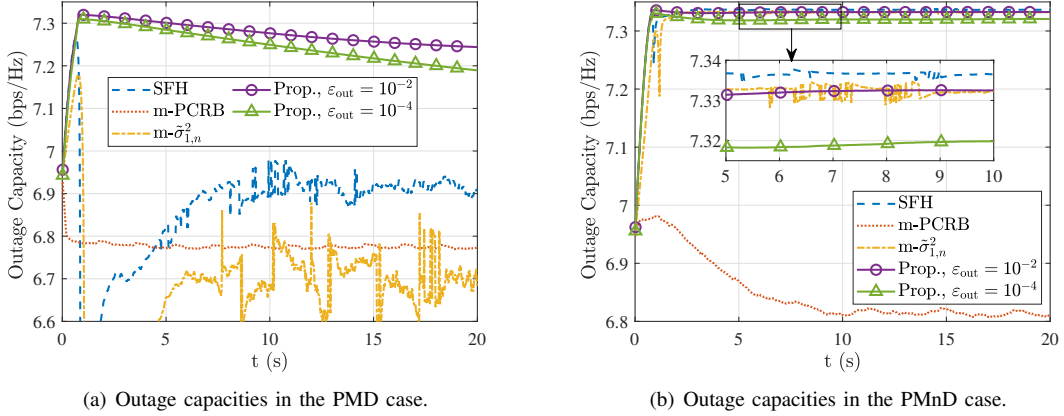


Fig. 7. Outage capacity comparisons among different schemes between the PMD and PMnD case.

PCRB scheme are relatively stable but limited by the high path loss. Comparatively, the outage capacity under our proposed scheme is much more stable than benchmarks and also higher than benchmarks for over 0.2 bps/Hz, which validates the effectiveness and superiorities of our proposed outage capacity maximization scheme over benchmarks in the PMD case. Nevertheless, Fig. 7(b) shows that such superiorities disappear in the PMnD case because the small measurement MSE leads to a low OP even if the UAV is close to the BS. Besides, the outage capacity under our proposed scheme in the case with $\varepsilon_{\text{out}} = 10^{-4}$ is lower than that with $\varepsilon_{\text{out}} = 10^{-2}$, which shows the trade-off between the communication reliability and efficiency.

VI. CONCLUSIONS

This paper studied the outage capacity maximization for UAV tracking enabled by sensing-assisted predictive beamforming, where the UAV trajectory, sensing duration ratio, and target constant received SNRs were jointly optimized. To facilitate the formulation of a tractable optimization problem, closed-form OP approximations were proposed based on second-order Taylor expansions, which also characterized the outage capacity. Then, two efficient algorithms were proposed to address the non-convex approximated optimization problem: a search-based algorithm with ensured convergence and an AO-based algorithm with lower complexity. Simulation results verified the effectiveness of our proposed approximations, algorithms, and the superiority of the proposed joint UAV tracking and outage capacity maximization scheme over benchmarks in the PMD case. Furthermore, our results demonstrated that the optimal predicted UAV trajectory tended to be parallel to the BS ULA antennas with a nonzero minimum distance, achieving a trade-off between decreasing path loss and increasing beam coverage area for outage capacity maximization. The extension of our proposed approximations to multi-static ISAC systems are worthwhile future works.

APPENDIX A PROOF OF PROPOSITION 1

According to the EKF framework [34], the state vector at each time slot can be approximately Gaussian distributed,

represented by $\mathbf{x}_{n-1} \sim \mathcal{N}(\check{\mathbf{x}}_{n-1}, \mathbf{M}_{n-1})$, $\forall n \in \{1, 2, \dots, N\}$. Thus, $\mathbf{x}_n \sim \mathcal{N}(\check{\mathbf{x}}_n, \mathbf{M}_{p,n})$ is derived from (3) and (9). Furthermore, as a marginal distribution of the state vector \mathbf{x}_n , the ground-truth UAV trajectory \mathbf{q}_n is also Gaussian distributed given by $\mathbf{q}_n \sim \mathcal{N}(\check{\mathbf{q}}_n, \check{\Lambda}_n)$ with

$$\check{\Lambda}_n = \begin{bmatrix} \check{\Lambda}_{x,n}^2 & \check{\Lambda}_{xy,n}^2 \\ \check{\Lambda}_{xy,n}^2 & \check{\Lambda}_{y,n}^2 \end{bmatrix} = \begin{bmatrix} [\mathbf{M}_{p,n}]_{11} & [\mathbf{M}_{p,n}]_{13} \\ [\mathbf{M}_{p,n}]_{31} & [\mathbf{M}_{p,n}]_{33} \end{bmatrix}. \quad (45)$$

Therefore, $\check{\mathbf{q}}_n \sim \mathcal{N}(\mathbf{0}, \check{\Lambda}_n)$ holds and the approximated OP at the prediction stage of the n th time slot (29) can be derived from the integral of $f(\check{\mathbf{q}}_n)$ on the complementary set of the aCOR (24), i.e.,

$$\zeta_{p,n} \approx \tilde{\zeta}_{p,n} = 1 - \int_{\check{x}_L}^{\check{x}_U} \left(\int_{\check{y}_L(\check{x}_n)}^{\check{y}_U(\check{x}_n)} f(\check{\mathbf{q}}_n) d\check{y}_n \right) d\check{x}_n, \quad (46)$$

where \check{x}_L and \check{x}_U can be obtained from the equation $d\check{x}_n/d\check{y}_n = 0$. This completes the proof.

APPENDIX B PROOF OF PROPOSITION 2

For notational simplicity, we adopt χ to represent either the function $\check{\chi}$ or $\hat{\chi}$. Accordingly, $\gamma, \bar{x}, \chi_U, \chi_L, \Lambda_{x,n}, \check{\Lambda}_n$ represents $\check{\gamma}_n, \check{x}_n, \check{\chi}_U, \check{\chi}_L, \check{\Lambda}_{x,n}, \check{\Lambda}_n$ in the case where χ denotes $\check{\chi}$, and $\hat{\gamma}_n, \hat{x}_n \hat{\chi}_U, \hat{\chi}_L, \hat{\Lambda}_{x,n}, \hat{\Lambda}_n$ in the case where χ denotes $\hat{\chi}$, respectively. Then, an upperbound of the partial derivative of χ w.r.t. γ can be derived as

$$\frac{\partial \chi}{\partial \gamma} \leq A \left(\frac{\partial Y_1}{\partial \gamma} + (\bar{x} + \check{x}_n)^2 \frac{\partial Y_2}{\partial \gamma} \right) = A\rho(\gamma), \quad (47)$$

with $A = \frac{\Lambda_{x,n} \max\{\frac{e^{-\chi_U(\gamma)}}{\sqrt{\pi}}, \frac{e^{-\chi_L(\gamma)}}{\sqrt{\pi}}\}}{\sqrt{2}|\det(\Lambda_n)|(Y_1 + Y_2(\bar{x} + \check{x}_n)^2)}$. The derivative of $\rho(\gamma)$ w.r.t. γ can be derived as $\frac{d\rho}{d\gamma} = \frac{(\check{x}_n^2 + \check{y}_n^2)^6 \tilde{P}(\rho_1 \gamma + \rho_0)}{((\check{x}_n^2 + \check{y}_n^2)^3 \gamma + \check{x}_n^2 \check{y}_n^2 \tilde{P} M)^4}$, where the specific expressions of ρ_0 and ρ_1 are given by

$$\rho_0 = 2\check{x}_n^2 \check{y}_n^2 \tilde{P} M (\check{y}_n^2 ((\check{x}_n + \check{x}_n)^2 (\check{x}_n^2 + 2\check{y}_n^2) + \check{x}_n^2 H^2) M + (\check{x}_n^2 + \check{y}_n^2)^3 N_t) \geq 0, \quad (48)$$

$$\rho_1 = 2\check{y}_n^2 (\check{x}_n^2 + \check{y}_n^2)^3 ((\check{x}_n + \check{x}_n)^2 (\check{x}_n^2 - \check{y}_n^2) + \check{x}_n^2 H^2) M + 2(\check{x}_n^2 + \check{y}_n^2)^6 N_t. \quad (49)$$

Next, two cases with $\rho_1 \geq 0$ and $\rho_1 < 0$ are discussed, respectively. For the case with $\rho_1 \geq 0$, $\frac{d\rho}{d\gamma} \geq 0$ holds due to $\gamma \geq 0$. As for the case with $\rho_1 < 0$, $\frac{d\rho}{d\gamma}$ is a

monotonically nonincreasing function. Since both $\frac{d\rho}{d\gamma}|_{\gamma=0} \geq 0$ and $\lim_{\gamma \rightarrow \infty} \frac{d\rho}{d\gamma} \geq 0$ can be obtained, $\frac{d\rho}{d\gamma} \geq 0$ also holds in this case. Thus, $\rho(\gamma)$ is a monotonically nondecreasing function of γ . Finally, both $\rho(0) \leq 0$ and $\lim_{\gamma \rightarrow \infty} \rho(\gamma) = 0$ can be obtained.

As a result, $\frac{\partial x}{\partial \gamma} \leq A\rho(\gamma) \leq 0$ holds, completing the proof.

REFERENCES

- [1] W. Khawaja *et al.*, “A survey on detection, classification, and tracking of UAVs using radar and communications systems,” *IEEE Commun. Surveys Tuts.*, pp. 1–1, early access 2025.
- [2] Q. Wu *et al.*, “A comprehensive overview on 5G-and-beyond networks with UAVs: From communications to sensing and intelligence,” *IEEE J. Sel. Areas Commun.*, vol. 39, no. 10, pp. 2912–2945, Oct. 2021.
- [3] Y. Wang *et al.*, “Toward realization of low-altitude economy networks: Core architecture, integrated technologies, and future directions,” 2025. [Online]. Available: <https://arxiv.org/abs/2504.21583>
- [4] Y. Jiang *et al.*, “Integrated sensing and communication for low altitude economy: Opportunities and challenges,” *IEEE Commun. Mag.*, pp. 1–7, early access 2025.
- [5] Y. Feng *et al.*, “Networked ISAC based UAV tracking and handover towards low-altitude economy,” *IEEE Trans. Wireless Commun.*, pp. 1–1, early access 2025.
- [6] Z. Wei, F. Liu, C. Masouros, N. Su, and A. P. Petropulu, “Toward multi-functional 6G wireless networks: Integrating sensing, communication, and security,” *IEEE Commun. Mag.*, vol. 60, no. 4, pp. 65–71, 2022.
- [7] F. Liu *et al.*, “Integrated sensing and communications: Toward dual-functional wireless networks for 6G and beyond,” *IEEE J. Sel. Areas Commun.*, vol. 40, no. 6, pp. 1728–1767, Jun. 2022.
- [8] F. Dong *et al.*, “Sensing as a service in 6G perceptive networks: A unified framework for ISAC resource allocation,” *IEEE Trans. Wireless Commun.*, vol. 22, no. 5, pp. 3522–3536, May 2023.
- [9] Y. Zhang *et al.*, “Toward throughput maximization of integrated sensing and communications enabled predictive beamforming for 6G,” *IEEE Netw.*, vol. 38, no. 4, pp. 292–300, Jul. 2024.
- [10] F. Liu *et al.*, “Radar-assisted predictive beamforming for vehicular links: Communication served by sensing,” *IEEE Trans. Wireless Commun.*, vol. 19, no. 11, pp. 7704–7719, Nov. 2020.
- [11] W. Yuan *et al.*, “Bayesian predictive beamforming for vehicular networks: A low-overhead joint radar-communication approach,” *IEEE Trans. Wireless Commun.*, vol. 20, no. 3, pp. 1442–1456, Mar. 2021.
- [12] X. Zhang, W. Yuan, C. Liu, J. Wu, and D. W. K. Ng, “Predictive beamforming for vehicles with complex behaviors in ISAC systems: A deep learning approach,” *IEEE J. Sel. Topics Signal Process.*, vol. 18, no. 5, pp. 828–841, Jul. 2024.
- [13] Z. Wang, V. W. Wong, and R. Schober, “Integrated sensing and communications for end-to-end predictive beamforming design in vehicle-to-infrastructure networks,” *IEEE J. Sel. Topics Signal Process.*, vol. 18, no. 5, pp. 933–949, Jul. 2024.
- [14] J. Mu *et al.*, “Integrated sensing and communication-enabled predictive beamforming with deep learning in vehicular networks,” *IEEE Commun. Lett.*, vol. 25, no. 10, pp. 3301–3304, Oct. 2021.
- [15] C. Liu *et al.*, “Learning-based predictive beamforming for integrated sensing and communication in vehicular networks,” *IEEE J. Sel. Areas Commun.*, vol. 40, no. 8, pp. 2317–2334, Aug. 2022.
- [16] W. Liang, Y. Wang, J. Zhang, L. Li, and Z. Han, “Predictive beamforming in integrated sensing and communication-enabled vehicular networks,” *IEEE Trans. Veh. Technol.*, vol. 74, no. 3, pp. 4539–4553, Mar. 2025.
- [17] H. Liu *et al.*, “Predictive ISAC beamforming using LoRA-transformer LSTM integrated with GNN in ultra-dense D2D mmWave networks,” *IEEE Trans. Veh. Technol.*, pp. 1–15, early access 2025.
- [18] Y. Zhang, S. Li, D. Li, J. Zhu, and Q. Guan, “Transformer-based predictive beamforming for integrated sensing and communication in vehicular networks,” *IEEE Internet Things J.*, vol. 11, no. 11, pp. 20690–20705, Jun. 2024.
- [19] X. Meng *et al.*, “Vehicular connectivity on complex trajectories: Roadway-geometry aware ISAC beam-tracking,” *IEEE Trans. Wireless Commun.*, vol. 22, no. 11, pp. 7408–7423, Nov. 2023.
- [20] Z. Du *et al.*, “Integrated sensing and communications for V2I networks: Dynamic predictive beamforming for extended vehicle targets,” *IEEE Trans. Wireless Commun.*, vol. 22, no. 6, pp. 3612–3627, Jun. 2023.
- [21] C. Yanpeng *et al.*, “Sensing-assisted accurate and fast beam management for cellular-connected mmWave UAV network,” *China Commun.*, vol. 21, no. 6, pp. 271–289, Jun. 2024.
- [22] J. Zhang *et al.*, “Deep learning-empowered secure predictive beamforming design for integrated sensing and communications systems,” *IEEE Trans. Wireless Commun.*, pp. 1–1, early access 2025.
- [23] A. A. Al-habob, O. A. Dobre, and Y. Jing, “Predictive beamforming approach for secure integrated sensing and communication with multiple aerial eavesdroppers,” *IEEE Trans. Commun.*, pp. 1–1, early access 2025.
- [24] X. Kang, Y.-C. Liang, A. Nallanathan, H. K. Garg, and R. Zhang, “Optimal power allocation for fading channels in cognitive radio networks: Ergodic capacity and outage capacity,” *IEEE Trans. Wireless Commun.*, vol. 8, no. 2, pp. 940–950, Feb. 2009.
- [25] A. Goldsmith, *Wireless communications*, Cambridge university press, 2005.
- [26] L. Liang, G. Y. Li, and W. Xu, “Resource allocation for D2D-enabled vehicular communications,” *IEEE Trans. Commun.*, vol. 65, no. 7, pp. 3186–3197, Jul. 2017.
- [27] Y. Zeng, Q. Wu, and R. Zhang, “Accessing from the sky: A tutorial on UAV communications for 5G and beyond,” *Proc. IEEE*, vol. 107, no. 12, pp. 2327–2375, Dec. 2019.
- [28] B. Chang, W. Tang, X. Yan, X. Tong, and Z. Chen, “Integrated scheduling of sensing, communication, and control for mmWave/THz communications in cellular connected UAV networks,” *IEEE J. Sel. Areas Commun.*, vol. 40, no. 7, pp. 2103–2113, 2022.
- [29] D. Xu, Y. Sun, D. W. K. Ng, and R. Schober, “Multiuser MISO UAV communications in uncertain environments with no-fly zones: Robust trajectory and resource allocation design,” *IEEE Trans. Commun.*, vol. 68, no. 5, pp. 3153–3172, May 2020.
- [30] M. A. Richards, *Fundamentals of Radar Signal Processing*, New York, NY, USA: McGraw-Hill, 2005.
- [31] Y. Jiang *et al.*, “UAV-enabled integrated sensing and communication: Tracking design and optimization,” *IEEE Commun. Lett.*, vol. 28, no. 5, pp. 1024–1028, May 2024.
- [32] Q. Wu, Y. Zeng, and R. Zhang, “Joint trajectory and communication design for multi-UAV enabled wireless networks,” *IEEE Trans. Wireless Commun.*, vol. 17, no. 3, pp. 2109–2121, Mar. 2018.
- [33] Y. Bar-Shalom, X. R. Li, and T. Kirubarajan, *Estimation with Applications to Tracking and Navigation*, New York, USA: Wiley, 2001.
- [34] S. M. Kay., *Fundamentals of Statistical Signal Processing, Volume 1: Estimation Theory*, Englewood Cliffs, NJ, USA: Prentice Hall, 1998.
- [35] J. Yan *et al.*, “Simultaneous multibeam resource allocation scheme for multiple target tracking,” *IEEE Trans. Signal Process.*, vol. 63, no. 12, pp. 3110–3122, Jun. 2015.
- [36] Q. Wu, J. Xu, and R. Zhang, “Capacity characterization of UAV-enabled two-user broadcast channel,” *IEEE J. Sel. Areas Commun.*, vol. 36, no. 9, pp. 1955–1971, Sep. 2018.
- [37] Y. Pan *et al.*, “Cooperative trajectory planning and resource allocation for UAV-enabled integrated sensing and communication systems,” *IEEE Trans. Veh. Technol.*, vol. 73, no. 5, pp. 6502–6516, May 2024.
- [38] P. Kumari, S. A. Vorobyov, and R. W. Heath, “Adaptive virtual waveform design for millimeter-wave joint communication–radar,” *IEEE Trans. Signal Process.*, vol. 68, pp. 715–730, Nov. 2019.
- [39] S. Boyd and L. Vandenberghe, *Convex Optimization*, Cambridge, U.K.:Cambridge Univ. Press, 2004.
- [40] Y. Sun, P. Babu, and D. P. Palomar, “Majorization-minimization algorithms in signal processing, communications, and machine learning,” *IEEE Trans. Signal Process.*, vol. 65, no. 3, pp. 794–816, Feb. 2017.
- [41] M. Grant and S. Boyd, “CVX: Matlab software for disciplined convex programming, version 2.1,” 2014. [Online]. Available: <http://cvxr.com/cvx>
- [42] J. Kim, H. Lee, C. Song, T. Oh, and I. Lee, “Sum throughput maximization for multi-user MIMO cognitive wireless powered communication networks,” *IEEE Trans. Wireless Commun.*, vol. 16, no. 2, pp. 913–923, Feb. 2017.
- [43] K. Meng, Q. Wu, W. Chen, and D. Li, “Sensing-assisted communication in vehicular networks with intelligent surface,” *IEEE Trans. Veh. Technol.*, vol. 73, no. 1, pp. 876–893, Jan. 2024.
- [44] Y. Jiang, Q. Wu, W. Chen, and H. Hui, “Energy-aware UAV-enabled target tracking: Online optimization with location constraints,” *IEEE Trans. Veh. Technol.*, vol. 74, no. 4, pp. 6668–6673, Apr. 2025.
- [45] G. Welch, G. Bishop *et al.*, *An introduction to the Kalman filter*. Chapel Hill, NC, USA, 1995.
- [46] K. Meng *et al.*, “Throughput maximization for UAV-enabled integrated periodic sensing and communication,” *IEEE Trans. Wireless Commun.*, vol. 22, no. 1, pp. 671–687, Jan. 2023.